




Regulated Ni–Zn–Co ferrites: structural, electrical and magnetic properties tailored by co doping

Armin Anwar^{1,*} , U. S. Akther², K. H. Maria¹, M. K. Alam³, A. Kumar⁴, and M. N. I. Khan⁴

¹ Department of Physics, University of Dhaka, Dhaka 1000, Bangladesh

² Green University of Bangladesh, Dhaka 1207, Bangladesh

³ Department of Physics, Bangladesh University of Engineering and Technology, Dhaka 1000, Bangladesh

⁴ Materials Science Division, Atomic Energy Centre, Dhaka 1000, Bangladesh

Received: 3 July 2023

Accepted: 1 December 2023

Published online:
21 December 2023

© The Author(s), under exclusive licence to Springer Science+Business Media, LLC, part of Springer Nature, 2023

ABSTRACT

In this investigation, synthesized Co substituted Ni-Zn ferrites $\{\text{Ni}_{0.6}\text{Zn}_{0.4-x}\text{Co}_x\text{Fe}_2\text{O}_4$ (for $x=0.00, 0.05, 0.10, 0.15, 0.20$) followed by double sintering method have been characterized by crystallographic, morphological, electrical and magnetic properties. X-ray diffraction (XRD) analysis as well as Fourier transform infrared (FT-IR) measurements of all the compositions verify the emergence of spinel cubic (single-phase) crystal structure. For Ni–Zn–Co ferrites, a cation dissemination has been suggested from the site occupancy preferences of different cations and its accuracy was confirmed by comparing the theoretically and experimentally computed lattice parameters as well as by measuring the magnetic moment. Scanning electron microscopy (SEM) showed diminished crystallite grains of average size 644 and 677 nm for 15% and 20% Co-doped compositions. An exceptional rise in dielectric constant for 10% Co-doped composite was observed at lower frequencies. AC conductivity of Co-doped ferrites showed that σ_{AC} decreases with increased Co content. A single incomplete semicircle for all the investigated compositions is observed in the Nyquist plot. The impedance and modulus spectrums analysis confirmed that Co substituted samples attain non-Debye kind dielectric relaxation. The maximum relaxation time τ of 4.19 μs was found for 20% Co-doped content. The 15% Co-doped composite exhibits a significant increment in saturation magnetization (87.39 emu/g) and in magnetic moment (3.69 μ_B). The value of initial permeability decreases noticeably with increased Co addition. Magnetic loss ($\tan\delta_M$) vs. frequency plot shows the beginning of relaxation peaks for all the NZCFO composites at higher ($> 10^7$ Hz) frequencies.

Address correspondence to E-mail: armin.phy@du.ac.bd

1 Introduction

Soft ferrimagnetic spinel Ni-Zn ferrites (NZFO) have proven beneficial in higher frequency implementations in a variety of industrial applications owing to their distinct characteristics like elevated electrical resistivity, superior Curie temperature, improved chemical and mechanical constancy, moderated magnetic induction, and minimal loss [1–5]. The properties of the inverse spinel of NiFe_2O_4 and normal spinel of ZnFe_2O_4 have merged to form mixed spinel Ni-Zn ferrite, which has the usual recipe of $(\text{Zn}_x\text{Fe}_{1-x})_{\text{tetra}}[\text{Ni}_{1-x}\text{Fe}_{1+x}]_{\text{octa}}\text{O}_4$. When Zn^{2+} ions with zero magnetic moment are swapped by magnetic Ni^{2+} ions, it can significantly impact the magnetic behaviors of ferrites as the characteristics are effectively susceptible to the cation allocation [6–9]. In the case of transition metals, generally, magnetic properties rely on the number of unpaired electrons of the 3d orbital. Ni^{2+} and Fe^{3+} ions have two and five unpaired electrons respectively in the 3d orbital, while Zn^{2+} ions possess only paired electrons in the 3d orbital [10–14]. Therefore, the relevant mixing of unpaired electrons of Ni^{2+} ion with zinc ferrite implements lower coercivity and higher magnetic saturation. The unpaired electrons of Ni^{2+} ions incite the relocation of a few Fe^{3+} ions from the octahedral [B]-sites to the tetrahedral (A)-sites. This creates an imbalance of Fe^{3+} ions among the lattice positions and thus improves magnetism. With these exceptional prospects, Ni-Zn ferrites are broadly employed in producing magnetic recording materials, elevated-frequency magnetic cores, loading coils, transformers, antenna rods, etc. [1–3, 15, 16]. Nevertheless, Ni-Zn ferrites possess low density, which poses its application in some other fields. For both theoretical and practical importance, these ferrites, especially their electrical properties, are regularly studied. Previous investigation has suggested that throughout the sintering progression, the loosing of Zn can create cation voidness as well as unsaturated oxygen ions. These newly produced excessive electrons can trigger bonding among the nearby Fe^{3+} ions, that later causes the increase of Fe^{2+} ions. This occurrence can induce the possibility of the jumping of electrons in octahedral sites inside the ferrite [17]. Interestingly, this hopping of $\text{Fe}^{3+} \leftrightarrow \text{Fe}^{2+}$ among (A) and [B] locations sometimes determine the electrical conduction as well as polarization inside the substances at high frequencies [18–20]. Moreover, respectively $\text{Fe}^{3+}/\text{Zn}^{2+}$ ratio at

(A) and $\text{Fe}^{3+}/\text{Ni}^{2+}$ ratio at [B] sites have an impact on the dielectric performance of NZFO [21].

It is challenging to synthesize materials with higher saturation magnetization, improved electrical resistivity, and elevated anisotropy, though such materials can be useful for practical applications. However, by doping with other metals such as chromium, copper, manganese, and cobalt, we can develop new ferrite materials with these desirable properties. For example, we can get better magnetic performance by doping the extremely resistive Ni-Zn ferrites with Co. The operation band of Ni-Zn-Co ferrite extends to a higher frequency than the undoped one, which means its magnetic permeability remains modest until the higher cut-off frequency region [22–25]. Cobalt-doped Ni-Zn ferrites become dense and possess moderated permeability and elevated Curie temperature along with high saturation magnetization, which is suitable for radiofrequency (RF) electronic device applications. Generally, Co^{2+} cations have a propensity to take place in both sites of NZFO, holding the majority of Co ions at the octahedral site [22]. When Co^{2+} ions appear at the B-site, they can positively contribute to the material anisotropy by restricting domain walls' movement and sharpening ferromagnetic resonance, consequently, a minimal loss is observed in Ni-Zn-Co ferrites (NZCFO). Moreover, ferrite microstructure is tailored by Co addition, which affects the electromagnetic performance of the developed ferrites [22, 23].

Several investigations have been published regarding the impact of adding Co to Ni-Zn ferrites [22–30]. However, there is a scarcity of detailed information on the redistribution of cations by cobalt substitution and its influence on several properties of NZCFO ceramics. In developing materials for MLCI applications, an investigation on cations' allocation across (A) and [B] sites could be useful. Moreover, for Co-substituted Ni-Zn composites, either magnetic or electrical features have been emphasized by most of the published studies. To obtain a thorough insight into the material, it may be beneficial to inspect both the electrical and magnetic performances synchronously as the cations have dissimilar ionic radii. Moreover, the higher magnetic moment of substituted Co^{2+} ($3 \mu_B$) ions can create a significant distortion of lattice within their vicinity, and thus, development in electrical as well as magnetic characteristics is anticipated. According to the literature, the $\text{Ni}_{0.5}\text{Zn}_{0.5}\text{Fe}_2\text{O}_4$ composition

exhibits the highest saturation magnetization [31]. However, the magnetic properties are notably altered by Zn doping; primarily, increases up to 0.4 and then decreases with a higher amount of doping, which was associated with preferential site occupancy [32]. Furthermore, Co addition improves the magnetic characteristic of Ni-Zn ferrites by initiating positive magnetocrystalline anisotropy into the composite [31]. Therefore, we aimed to develop $\text{Ni}_{0.6}\text{Zn}_{0.4-x}\text{Co}_x\text{Fe}_2\text{O}_4$ composition by varying Co concentration in place of Zn while keeping Ni fixed at 0.6 mol, applying the double sintering method. Also, an attempt was made to analyze the variation in structural, electrical, and magnetic parameters with reference to microstructural changes based on the reallocation of Co^{2+} ions across (A) and [B] locations in the NZFO system.

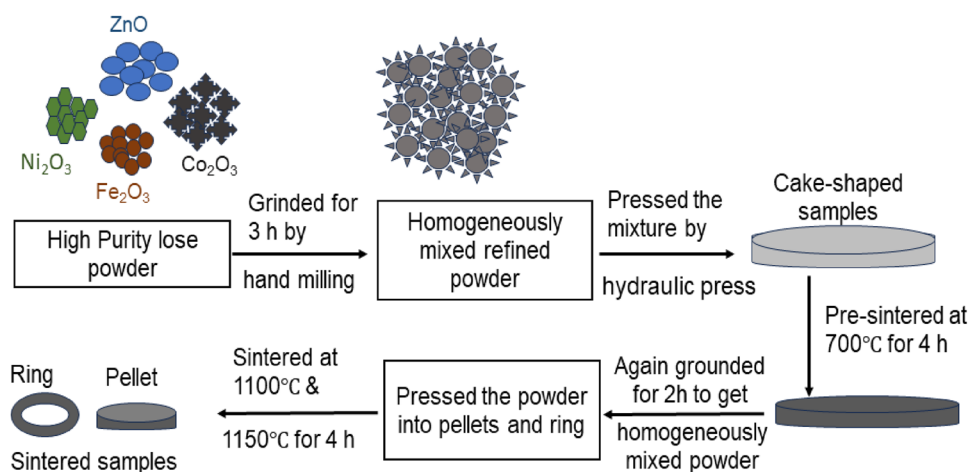
2 Experimental details

A standard double sintering technique was adopted to formulate polycrystalline Co-doped spinel $\text{Ni}_{0.6}\text{Zn}_{0.4-x}\text{Co}_x\text{Fe}_2\text{O}_4$ (for $x = 0.00, 0.05, 0.10, 0.15, 0.20$) compositions. Commercially available analytical raw compounds of Ni_2O_3 , ZnO , Co_2O_3 , and Fe_2O_3 with higher clarity were weighed accurately in required stoichiometric proportions. In an agate mortar, these ingredients were grounded for 3 h continuously to form a homogeneous mixture. A cake-shaped form was created by pressing this mixture tightly employing a hydraulic press which afterwards was pre-sintered at 700°C for 4 h using a programmable furnace. After taking it out from the furnace, all the specimens were crushed and re-grounded again to

improve the proportion of homogeneity. As a binder, a slight measure of 5% polyvinyl alcohol was mixed with powder to fabricate ring and disk-shaped samples at 10 kN pressure using the uniaxial compressor. The ring-shaped samples have an outer diameter of 8.5 mm, an inner diameter of 6.5 mm with a thickness of about 2.5 mm, and disk-shaped pellets are 8.5 mm diameter with 2.5 mm thickness. Then, after setting a holding time of 4 h, the pellet-shaped specimens were sintered with two separate 1100°C and 1150°C temperatures for transforming the powder materials into densely compact grains. Finally, the crystallographic, microstructural, electrical, and magnetic attributes of $\text{Ni}_{0.6}\text{Zn}_{0.4-x}\text{Co}_x\text{Fe}_2\text{O}_4$ ferrites were investigated using these sintered pellets and the ground powders. A flow chart diagram of sample formulation is displayed in Fig. 1.

The phase development of all synthesized NZCFO specimens was explored through their XRD patterns by using the Philips PW 3040 X'Pert Pro X-ray powder diffractometer, where Cu-K_α radiation (with $\lambda = 0.154\text{nm}$) was used in the scattering range (2θ) of 20° to 70° . The theoretical (a_{th}) and experimental (a_{expt}) lattice parameter, bulk density (ρ_B), x-ray density (ρ_X), porosity (P), crystallite size (D) and strain (ϵ) were determined from X-ray diffraction spectrums. The scanning electron microscopy (known as SEM) has facilitated examining in detail the morphological as well as microstructural features of the fabricated specimens at room temperature (RT). Applying ImageJ software, the grains' magnitude, and the dissemination outline were analyzed. Moreover, to reveal the crystal structure of all the compositions at RT, Fourier Transforms Infrared (FTIR) spectrum

Fig. 1 Procedure of $\text{Ni}_{0.6}\text{Zn}_{0.4-x}\text{Co}_x\text{Fe}_2\text{O}_4$ sample preparation via standard double sintering technique



ranging from 4000–400 cm^{-1} (wave number) was documented. This study was conducted by inserting the samples in the solution of potassium bromide (KBr), utilizing a spectrophotometer named Shimadzu FTIR 8400 S (Japan). All the examined spectra have been rectified for background elements appearing from the air. For investigating dielectric and electrical behavior (AC conductivity, impedance, and modulus spectrums), all the manufactured pellets were smoothed so that the surfaces of both sides were parallelly aligned. Then, to confirm high-quality electrical contact, the opposite faces of each pellet of undoped and Co-doped samples were covered with conducting silver paste, where the ferrite materials act as a dielectric medium. The dielectric response (dielectric constant (ϵ) and dielectric loss ($\tan\delta$)), AC conductivity (σ_{AC}), complex impedance (Z), electric modulus (M), initial permeability (μ'_i) and relative quality factor (RQF) of the sintered specimens were studied at RT with respect to frequency variation ranging from 10^2 to 10^8 Hz using Wayne Kerr 6500B precession impedance analyzer, monitored by a computer. Moreover, utilizing an EV9 micro sense Lake Shore VSM (vibrating sample magnetometry) magnetic characterization was monitored.

3 Results and discussion

3.1 Structural analysis

X-ray diffraction analysis spectra of $\text{Ni}_{0.6}\text{Zn}_{0.4-x}\text{Co}_x\text{Fe}_2\text{O}_4$ composites at 1100 and 1150 °C distinct sintering temperatures are presented in Fig. 2a, b. It is apparently noticeable from these two illustrations that with the augmentation of heat treatment from 1100 to 1150 °C, the diffraction peaks of all the samples reflect very highly intensified and sharper peaks, indicating a comparatively better crystallized structure. Moreover, the inset of Fig. 2a shows that for all the composites, the parting of (311) plane around 35° for 1100 °C sintering temperature is hardly visible in the XRD spectrums for 1150 °C. This offers evidence of having the perfect spinel structure with Fd3m space group [18] for the NZCFO specimens prepared at 1150 °C. The outcome also reveals that densification during the sintering process may not have finished for the synthesized samples at 1100 °C. Due to these reasons, in our investigation, all the characterizations were performed for the compositions sintered at 1150 °C

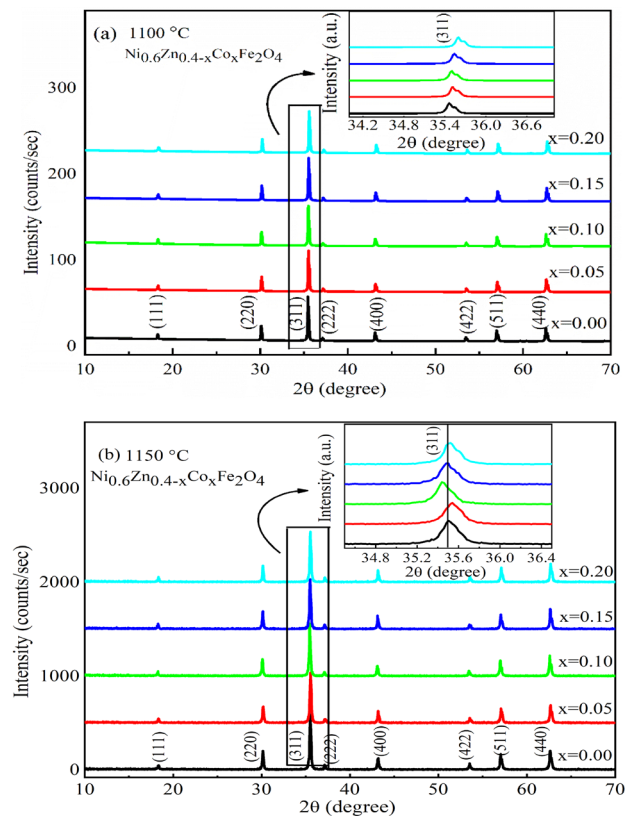


Fig. 2 XRD patterns of Co-doped $\text{Ni}_{0.6}\text{Zn}_{0.4-x}\text{Co}_x\text{Fe}_2\text{O}_4$ at two distinct sintering **a** 1100 °C and **b** 1150 °C temperatures

temperature. For pure Ni-Zn ferrite, the distinguishable diffracted peaks of (111), (220), (311), (222), (400), (422), (511), and (440) planes are well-fitted with the standard reference data (JCPDS Card no. 52-0278) [16, 33]. As it is visible from Fig. 2b, all the Co-doped composites demonstrate the development of spinel cubic (single-phase) crystal structure like the undoped one without some signs of the secondary phases, indicating the structure of NZCFO crystals stays the same.

To firmly inspect the peak position with different concentrations of Co doping, the enlarged view of X-ray diffraction patterns from 34.5° to 36.5° is demonstrated in Fig. 2b (inset). The most intense peak (311) for 5% and 10% Co-doped composites are apparently shifting to higher and lower diffraction angles, respectively. This implies that with Co substitution the lattice constant has probably reduced and then again improved. It was proposed that when ions of dissimilar ionic radii are doped it could produce strain within the lattice. One is the compressive strain that drifts the peak position toward larger angles, another one is the tensile strain

intensification which moves the peak to lower angles [34].

By considering all the diffracted planes, lattice constant was determined for all NZCFO samples applying the equation:

$$a = d_{hkl} \sqrt{h^2 + k^2 + l^2} \tag{1}$$

where d_{hkl} is the separation between the crystal planes]. These estimated lattice parameters 'a' were plotted against Nelson-Riley function [35]:

$$F(\theta) = \frac{1}{2} \left(\frac{\cos^2\theta}{\sin^2\theta} + \frac{\cos^2\theta}{\theta} \right) \tag{2}$$

where the experimental a_{expt} values were found out from the interception of lattice parameter vs. $F(\theta)$

curves. As an exemplary among all the composites, the 'a' value associated with all the diffracted planes were plotted against $F(\theta)$ for $x = 0.15$ and depicted in Fig. 3a. Now, it should be remarked that for spinel ferrites the structural and magnetic behaviors are built upon the placement of different sized cations over (A) and [B] positions. Therefore, it is requisite to understand the dissemination of cations as well as spin alignment to figure out the actual magnetic properties of spinel ferrite. As Zn^{2+} is non-magnetic, in spinel ferrites, it prefers to take place at A-sites while magnetic Ni^{2+} goes to B-sites. Whereas Co^{2+} ions can reside on both positions like Fe^{3+} ions. 10% of introduced Co^{2+} ions get-into A-sites to take the place of zinc ions and 90% of them reside in octahedral sites by switching Fe^{3+} ions toward tetrahedral sites [23].

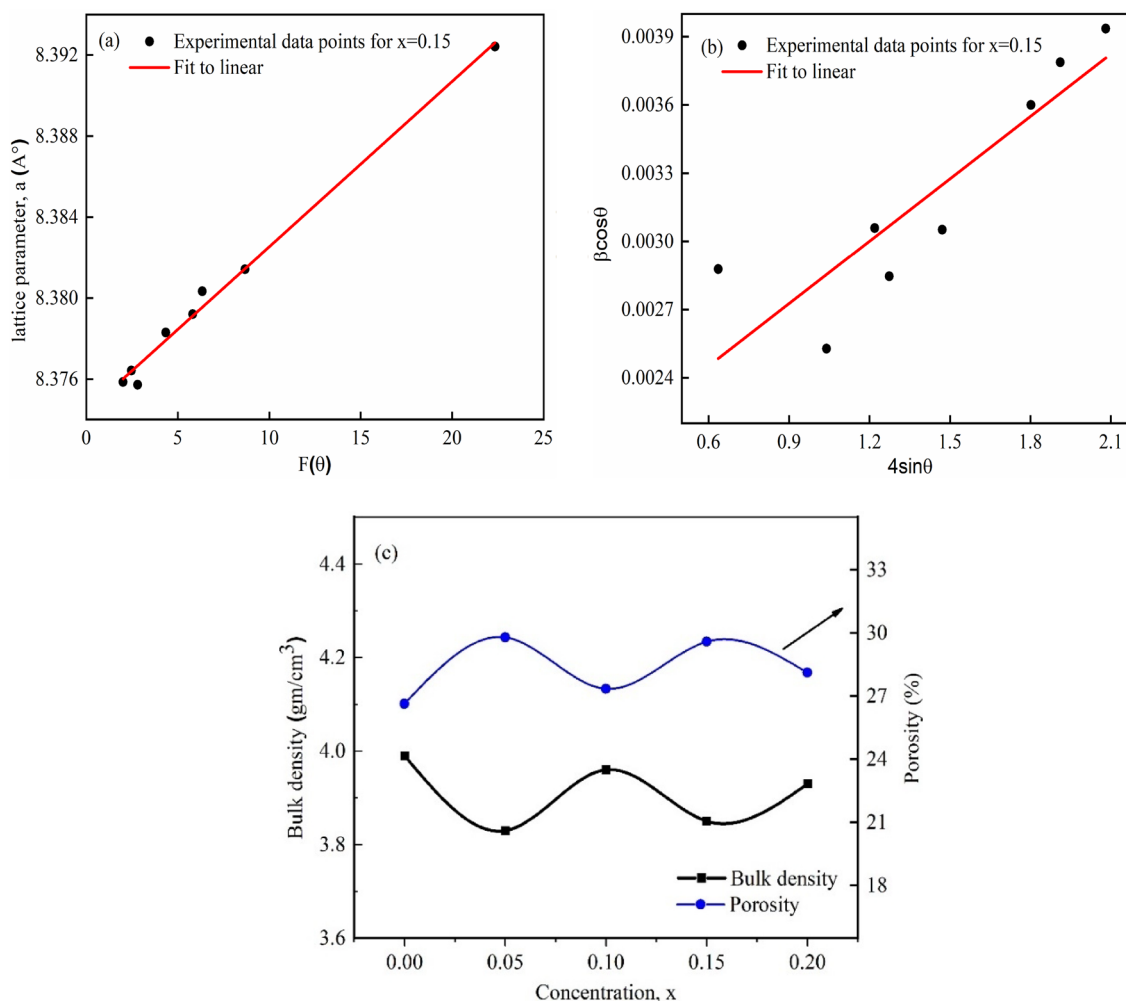
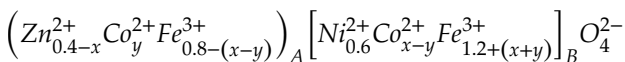


Fig. 3 a Lattice parameter vs. Nelson–Riley function; b Williamson–Hall plot for $x = 0.15$ composition and c variation of ρ_b and $P(\%)$ of Co doped $Ni_{0.6}Zn_{0.4-x}Co_xFe_2O_4$ ferrites

Based on ions occupancy at different sites, a successive cation distribution can be proposed to interpret the characterization results of our samples:



For Ni–Zn–Co ferrites, the theoretically computed lattice parameters (a_{th}) can assure the accuracy of the suggested cations’ sharing by following relations:

$$a_{th} = \frac{8}{3\sqrt{3}} \left[(r_A + R_0) + \sqrt{3}(r_B + R_0) \right] \tag{3}$$

$$r_A = (0.4 - x)r_{Zn} + yr_{Co} + \{0.8 - (x - y)\}r_{Fe} \tag{4}$$

$$r_B = \frac{1}{2} [0.6r_{Ni} + (x - y)r_{Co} + \{1.2 + (x - y)\}r_{Fe}] \tag{5}$$

Here, $R_0 = 1.38 \text{ \AA}$ is the radius of oxygen ion [36], and r_A and r_B are the respective ionic radii of (A) and [B] sites; whose estimates are related to the distribution of cations. In Table 1, a side-by-side comparison of the theoretical standards and the experimentally computed lattice parameters are illustrated. The evaluated a_{expt} values reveal that the XRD peaks decline with the addition of 5% Co content and then start to rise for 10% Co concentration and finally drops again with further Co addition. Whereas the calculated a_{th} values illustrate a continuous decreasing tendency with the augmentation of Co addition. Crystallite size as well as strain of all compositions have also been computed using the W-H (Williamson-Hall) approach (Eq. 6 [37]):

$$\beta \cos \theta = k\lambda/D + 4\epsilon \sin \theta \tag{6}$$

where λ is the wavelength ($= 1.54 \text{ \AA}$) of Cu-K α radiation, $\theta =$ Bragg’s angle and β (in radians) is the peaks’ FWHM. Figure 3b displays the linear fitted W-H plot for 15% sample, where the positive gradient points out a presence of tensile strain within the corresponding sample. It is apparent from Table 1 that 5% Co introduction doesn’t show any significant change in the crystallite size (D) compared to undoped one, but with 10% doping, D has amplified noteworthy. This may have been caused because of the deviation of diffracted peaks towards low range angle and the increased internal strain. Again, the crystallite size

Table 1 Cation distributions, ionic radii, lattice constants, bulk and x-ray densities, porosity, crystallite size and strain of $Ni_{0.6}Zn_{0.4-x}Co_xFe_2O_4$ ferrites

Composition	Cation distribution		Ionic radii		Theoretical lattice constant a_{th} (Å)	Lattice parameter from N–R function a_{expt} (Å)	Bulk density ρ_B (g/cm ³)	X-ray density ρ_x (g/cm ³)	Porosity P (%)	Crystallite size D (nm)	Strain ϵ ($\times 10^{-3}$)
	A-site	B-site	r_A (Å)	r_B (Å)							
$x=0.00$	$(Zn_{0.4}^{2+}Fe_{0.80}^{3+})_A$	$[Ni_{0.6}^{2+}Fe_{1.2}^{3+}]_B$	0.688	0.594	8.377	8.375	3.99	5.44	26.63	68	0.806
$x=0.05$	$(Zn_{0.35}^{2+}Co_{0.005}^{2+}Fe_{0.76}^{3+})_A$	$[Ni_{0.6}^{2+}Co_{0.045}^{2+}Fe_{1.24}^{3+}]_B$	0.632	0.623	8.371	8.369	3.83	5.45	29.79	69	0.864
$x=0.10$	$(Zn_{0.30}^{2+}Co_{0.01}^{2+}Fe_{0.71}^{3+})_A$	$[Ni_{0.6}^{2+}Co_{0.09}^{2+}Fe_{1.29}^{3+}]_B$	0.576	0.652	8.382	8.389	3.96	5.45	27.34	110	1.230
$x=0.15$	$(Zn_{0.25}^{2+}Co_{0.015}^{2+}Fe_{0.67}^{3+})_A$	$[Ni_{0.6}^{2+}Co_{0.135}^{2+}Fe_{1.33}^{3+}]_B$	0.520	0.681	8.374	8.380	3.85	5.46	29.58	76	0.915
$x=0.20$	$(Zn_{0.20}^{2+}Co_{0.02}^{2+}Fe_{0.62}^{3+})_A$	$[Ni_{0.6}^{2+}Co_{0.18}^{2+}Fe_{1.38}^{3+}]_B$	0.464	0.710	8.371	8.373	3.93	5.47	28.11	95	1.102

decreases for 15% Co doped composition and then starts to rise again with further Co addition. The abrupt increment and decrement of the structural parameters such as D and a_{expt} with the cobalt doping maybe linked to the variation of cation distributions at A and B positions. The slightly diminished crystallite size at $x = 0.05$ and 0.15 has been expected because of the distributional effect on (A) and (B) sites with cations of different ionic radii of Co^{2+} ($= 0.65 \text{ \AA}$) and Zn^{2+} ($= 0.74 \text{ \AA}$). As it was remarked beforehand that in Ni-Zn ferrite structure, Co^{2+} ions mostly favor B sites. Up to 15% Co doping, some Zn^{2+} ions at site (A) are substituted by Co and probably an equivalent Zn^{2+} ions occupy the octahedral site as a replacement of Ni^{2+} ($= 0.69 \text{ \AA}$), which creates a small-scale contraction in the unit cell and therefore, triggers a reduction in D as well as a_{expt} [23]. Similar works have reported that since Co can randomly substitute the two cations at A- and B- sites, it causes an unsystematic variation and insignificant difference in the lattice constant [38, 39]. Furthermore, the tensile strain was found to enhance prominently at $x = 0.10$ and $x = 0.20$ which is believed to have originated due to lattice distortion. Again, the distinctions in Co^{2+} and Zn^{2+} ionic radii could generate lattice strains, introducing inner stress that can impede the growth of grains [40, 41].

The bulk density ($\rho_B = \frac{m}{\pi r^2 h}$; here, r , h denote the pellets' radius and depth and m is their mass) of all the NZCFO specimens as well as the x-ray density ($\rho_X = \frac{ZM}{N_A a^3}$; where M = molecular weight, atomic number $Z = 8$ for cubic spinel ferrite, and N_A is Avogadro's number) have been displayed in Table 1. The density plays a vital role for ferrite compositions since it governs the magnetic properties. It has been suggested by previous researchers that for ferrites, the increased density can be obtained if the permeability is higher. From Table 1, it is obvious that with a small addition of 5% Co the densification mechanism has demoted significantly, while further inclusion ($> x = 0.05$) of Co has improved densification and hence boosted ρ_B . Moreover, the dissimilarity between atomic weights of Co and Zn (Co^{2+} (58.93 amu) $<$ Zn^{2+} (65.38 amu)) may have helped to increase ρ_B for 10% and 20% Co doped samples. As for x-ray density, a proportional but subtle increment with the increasing Co substitution was observed.

It is also prominent from Table 1 that ρ_B values are reduced in magnitude compared to ρ_X values. Doping with 5% and 15% Co^{2+} ions have notably

diminished the bulk density which may have triggered due to the hampered mass transportation throughout the sintering procedure, which causes the enlargement of intergranular/intragranular porosity [42, 43]. Therefore, a change in the interatomic distances occurs, which can contribute to the enlargement of unit cell volume and thus, diminishes the density. Figure 3c exhibits an inversely proportional behavior of bulk density and porosity ($P(\%) = \frac{\rho_X - \rho_B}{\rho_X} \times 100\%$) with the increased Co addition, which is analogous to the formerly reported research outcome [33]. It is noticeable that for $x = 0.0$ composition, ρ_B is 3.99 g/cm^3 and P is 26.63% which are the highest and lowest among all the compositions. Sometimes the discontinuous progress of grains can hamper the movement of pores toward the grain boundary [44] which promotes the intergranular porosity and thus, reduces ρ_B .

Figure 4 displays the FTIR spectra of NZCFO systems with varied Co substitution which were recorded between 400 and 4000 cm^{-1} at RT. The two strong peaks around $588.29\text{--}690.22 \text{ cm}^{-1}$ (ν_1) and $394.85\text{--}405.58 \text{ cm}^{-1}$ (ν_2) are observed in each sample which confirm the spinel configuration of our studied specimens [38, 45]. The bands at ($588.29\text{--}690.22 \text{ cm}^{-1}$) correspond to the $\text{Fe}^{3+}\text{--O}^{2-}$ bonds' stretching vibration in (A) positions and due to the chemical bonds among the oxygen ions, whereas the bands around ($394.85\text{--}405.58 \text{ cm}^{-1}$) signify the octahedral site metal cations vibration [46]. The frequency variation in these

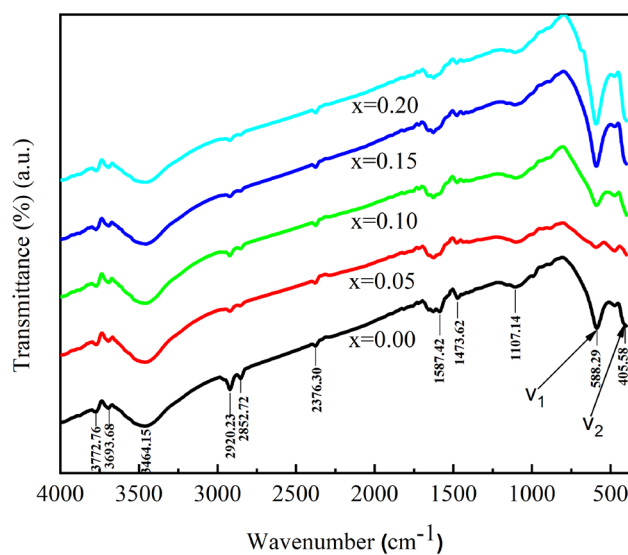


Fig. 4 FTIR spectra of $\text{Ni}_{0.6}\text{Zn}_{0.4-x}\text{Co}_x\text{Fe}_2\text{O}_4$ ferrite systems

two peaks with Co doping is related to the cations' mass as well as the separation between oxygen and cations, whereas the frequency of chemical bonds is influenced by their binding force. Here, in the case of the undoped sample ($\text{Ni}_{0.6}\text{Zn}_{0.4}\text{Fe}_2\text{O}_4$), the band for tetrahedral sites arises in 588.29 cm^{-1} . On the other hand, the bands of Co doped samples $\text{Ni}_{0.6}\text{Zn}_{0.4-x}\text{Co}_x\text{Fe}_2\text{O}_4$ ($x = 0.05, 0.10, 0.15, 0.20$) forms at $592.15, 588.29, 590.22$ and 592.15 cm^{-1} respectively. Similarly, for octahedral sites, the band shifts from 405.58 to $395.68, 394.85, 395.68$ and 400.63 cm^{-1} respectively, for Co doped ferrites. Interestingly, the bands around ν_1 and ν_2 are observed to move slightly towards higher and lower frequency zone with enhanced Co doping. Added Co^{2+} ions strongly show a propensity to reside at [B] location, whereas the interchanged Fe^{3+} ions will migrate to the tetrahedral site, which affects the absorption frequency. Therefore, this small change in band position is believed to be the reason for relocating the A- and B- sites' cations in NZCFO ferrites. This also validates that the crystal configuration stays in spinel cubic phase even though Zn was replaced by Co in Ni-Zn ferrite. The very analogous behavior was informed in Cu substituted Co-Ni ferrite systems [45]. The residual C-O bonds' vibration may have caused the appearance of bands around 1107.14 to 1109.07 cm^{-1} . Whereas the vibration due to C-H stretching initiates absorption band around 1473.62 to 1477.47 cm^{-1} . The bending mode of water (H-O-H) is noticed at around 1587.42 cm^{-1} for undoped ferrite, and for Co doped ferrites, it slightly shifted to 1625 cm^{-1} . The peaks around 2376.30 cm^{-1} are identified for all the samples, which are assigned to symmetric and asymmetric C=O modes, correspondingly [47]. The double peaks detected around 2852 as well as 2922 cm^{-1} for all samples may have arisen due to the C-H symmetric stretching and antisymmetric stretching of $-\text{CH}_2-$ group. A broad hump is observed around 3464 cm^{-1} due to H-O-H stretching [48, 49]. Within the interval of $3772-3693\text{ cm}^{-1}$, the observed bands are correlated with vibrations of C=C bonds.

The synthesized Ni-Zn-Co ferrites were further characterized by SEM analysis for morphological and grain size distribution information, whose images are presented in Fig. 5a-e along with their respective histograms. With varying Co concentration, the grain growing process and their different sizes impact significantly on the magnetic behavior. The observed morphology and microstructure of undoped and Co doped composites indicate that they are very

analogous to each other, and the grains are in spherical and polygonal shape with a high degree of intergranular voids. Since all the specimens were subjected to a 4 h lengthy sintering action, the insufficiency of activation energy can restrain the mobility of grain boundary. This may cause an impediment of grain development mechanism yet preserving the dispersion of grain boundary functional [50, 51].

It was advised that in solid state reaction process, an appropriate sintering temperature could minimize the presence of pores, which diminishes grains' size and thus, can aid the suppression of grain boundaries [43]. SEM micrograph of the undoped $x = 0.00$ sample has demonstrated that the microstructure contains non-homogenous and clearly separated unsymmetric shaped grains of 866 nm average size. With the slightest addition ($x = 0.05$) of Co, polyhedral shaped grains were viewed with reduced average grain size (824 nm), while presenting a fewer porous configuration. But it is visible from the images that with the further augmentation of Co^{2+} ions, the feature of micrographs has become more sharpened along with agglomerated grains. The surface morphology of 10% and 15% Co substituted Ni-Zn ferrites, with marginally diminished grains of average size 735 nm and 644 nm has distinguishably degraded, whereas for 20% Co doped composition, the average size has increased a little to 677 nm . As it is well-established, the $\text{Co}^{2+}-\text{O}^{2-}$ bonding has greater energy (368 kJ/mole) compared to the $\text{Zn}^{2+}-\text{O}^{2-}$ bonding (284 kJ/mole). Therefore, to formulate $\text{Co}^{2+}-\text{O}^{2-}$ bonds, extra energy is required for forcing Co ions to get in the Ni-Zn lattice system. That is, in order to complete the grain growth and crystallization for Co^{2+} ions substituted in ferrites, additional energy will be required to create smaller sized ferrite grains. On the other hand, mass transportation is largely obstructed by Co addition, which affects the densification of ferrite compositions. Consequently, an increased porosity has been identified in Co doped compositions in contrast with the undoped one [42]. This occupancy of noticeable number of intergranular pores (open pores) may act as the source of larger demagnetization, which weakens the domain walls movement in NZCFO ferrite grains volume. Hence, the presence of open pores in the composites can be accountable for the weakening of magnetization saturation.

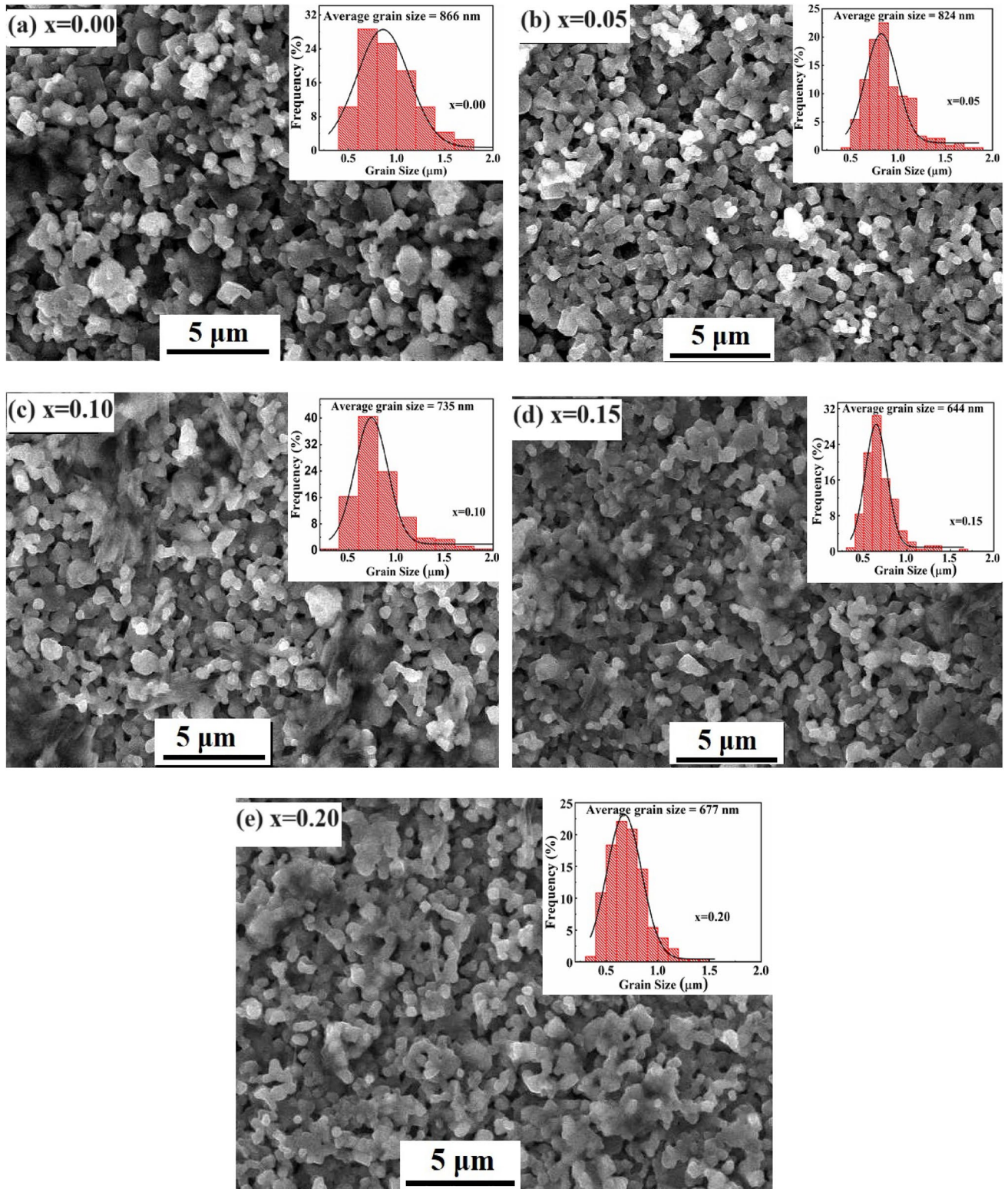


Fig. 5 SEM images and the corresponding histograms of $\text{Ni}_{0.6}\text{Zn}_{0.4-x}\text{Co}_x\text{Fe}_2\text{O}_4$ ($0 \leq x \leq 0.2$) ferrites at 5000 \times magnification with 20 kV

3.2 Dielectric measurements

Spinel ferrites' dielectric performance strongly depends on cation distributions, composition or stoichiometry, method of synthesis, grain size, bulk density, particle size, microstructure homogeneity and sintering temperature [52, 53]. The dielectric responses (expressed by complex dielectric constant, $\epsilon^* = \epsilon' - \epsilon''$) of $\text{Ni}_{0.6}\text{Zn}_{0.4-x}\text{Co}_x\text{Fe}_2\text{O}_4$ ($0 \leq x \leq 0.2$) solid samples with frequency variation (approximately 10^2 – 10^8 Hz) have been examined at RT and are illustrated in Fig. 6a, b.

The stored energy in dielectric is represented by the real part, ϵ' of ϵ^* and the energy loss is denoted

by the imaginary part, ϵ'' . After analyzing both figures, it is obvious that among all the compositions, Co undoped ($x = 0.00$) sample at lower frequencies displays the highest ϵ' and ϵ'' . In general, for every NZCFO composite, the dielectric constant exhibits fast decay as the frequency is increased but later it is hardly dependent on the external field at higher frequency area, which is expected in dielectric spinel ferrites. Similar dielectric behavior for Ni-Zn ferrites with different doping elements (Gd, Sr, Sn) has been reported previously [30, 44, 54]. The reliance of ϵ' on frequency can be explained using the Debye equation:

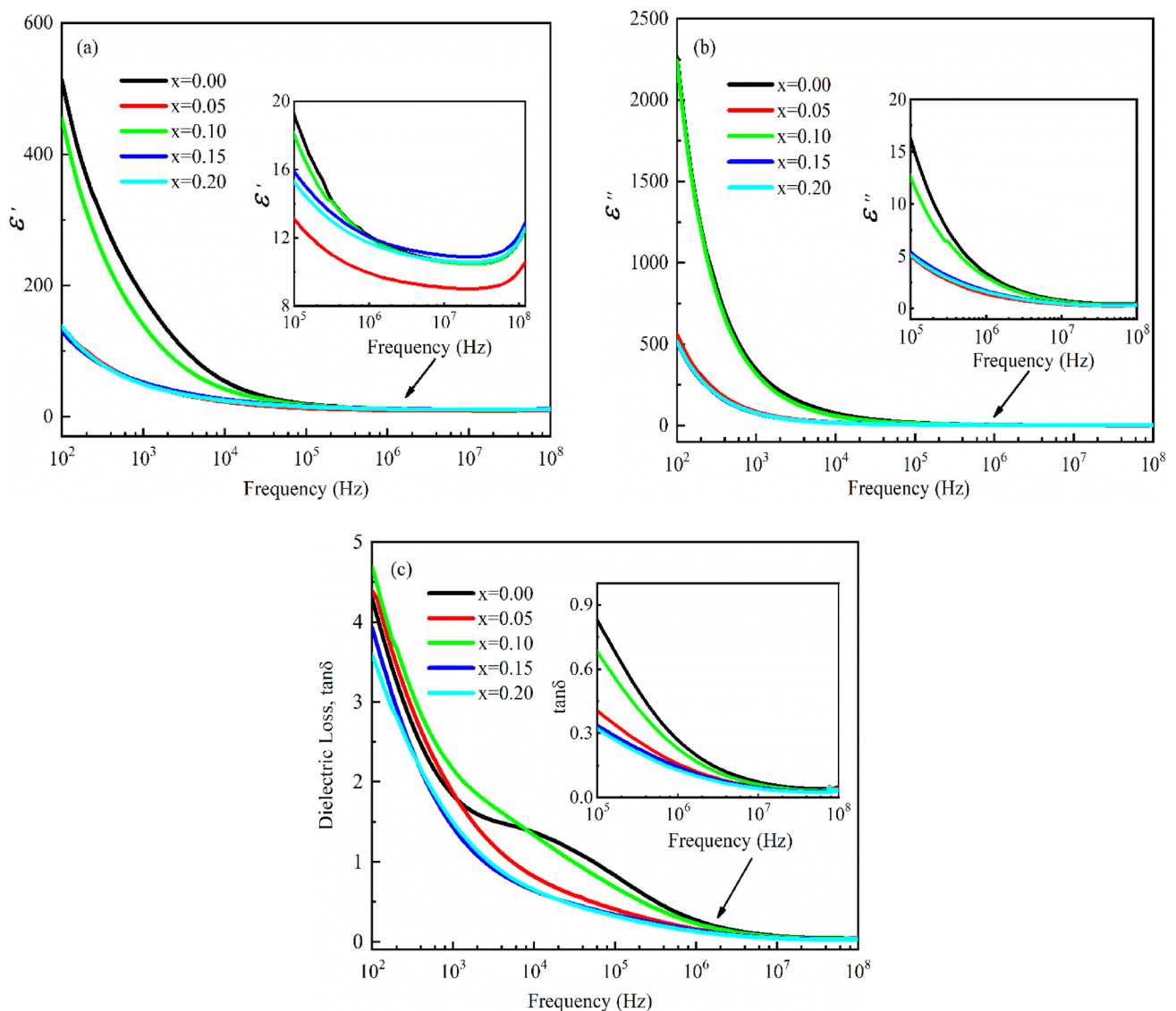


Fig. 6 Dielectric behavior: **a** real (ϵ') and **b** imaginary parts (ϵ'') of dielectric constant and **c** dielectric loss ($\tan\delta$) against frequency for $\text{Ni}_{0.6}\text{Zn}_{0.4-x}\text{Co}_x\text{Fe}_2\text{O}_4$ ferrites at RT

$$\epsilon' = \epsilon_{\infty} - \frac{\epsilon_0 - \epsilon_{\infty}}{1 + \omega^2 \tau^2} \quad (7)$$

where ϵ_{∞} and ϵ_0 are the dielectric constants for very high and very low frequencies, τ denotes the relaxation time. At the lower-frequency section, dielectric constant is impacted by interfacial and ionic polarization, whereas in the upper-frequency domain, contribution to ϵ' comes from electronic and dipolar polarization. Various kinds of defects might have been created throughout the sample formulation and sintering, which activates interfacial polarization to dominate in ferrites. According to Koop's theory, grains in ferrites are perfectly conducting. Whereas the development of weakly conducting grain boundaries during the sintering procedure because of the oxidation or apparent diminution of crystallites by means of their immediate interaction with atmospheric firing isolates the conducting grains [55, 56]. Now, the external field influences the charge carriers to move at low frequencies but because of the badly conducting boundaries, the charge carriers with high enough resistances align themselves parallelly to the grain boundaries. Consequently, this aggregation of confined charges increases the interfacial polarization, which accelerates an improved dielectric constant at lower frequency area [57]. Meanwhile, within the higher-frequency domain, the inability of space or interfacial charges in following the very rapidly oscillating field due to inertia contributes to the decrement of ϵ' .

Interestingly, the inset of Fig. 6a displays that at the opposite end of the frequency spectrum ($> 10^7$ Hz), ϵ' of all the samples start to show a sudden response with the applied field. Some early studies [58, 59] have mentioned that electrons with light mass, beyond the infrared region, can still pursue the field which confirms the existence of electronic polarizability. Another declaration can be made from Fig. 6a and b that both ϵ' and ϵ'' diminish significantly (except for $x = 0.10$) with the Co addition. There are probably two conduction mechanisms in Ni-Zn ferrite system: one is electron jumping among Fe^{2+} and Fe^{3+} ions, another one is hole hopping among Ni^{2+} and Ni^{3+} ions. As Co cations have a high tendency to inhabit B-sites in contrast to A-sites, subsequently, with the increasing Co concentration, Ni starts to get replaced at octahedral sites which heightens the presence of a large amount of Fe^{3+} ions [55]. Therefore, these conduction mechanisms probably

reduce the interfacial polarization buildup earlier and hence, a diminution in ϵ' follows with elevated Co concentration. An analogous outcome was also detected in other ferrites [60, 61]. The exceptional rise in ϵ' for 10% Co doped composite at lower frequencies may have been caused due to the changes in structural uniformity. These modifications may have resulted in larger lattice parameter value and improved bulk density as we have observed in XRD section, and this leads to a diminution in the degree of polarization.

Figure 6c illustrates the dependency of loss factor ($\tan \delta = \frac{\epsilon''}{\epsilon'}$) on frequency for Co doped $\text{Ni}_{0.6}\text{Zn}_{0.4-x}\text{Co}_x\text{Fe}_2\text{O}_4$ systems. For all the specimens at lower frequency domain, $\tan \delta$ is evidently higher which later with the increased frequency starts to fall sharply and this behavior agrees with the Koop's phenomenological theory [62]. Changes in microstructure or imperfections in lattice, the presence of magnetostriction and anisotropy can strongly influence the loss. At lower frequency ranges, electric field frequency is significantly smaller in comparison to the $\text{Fe}^{2+} \leftrightarrow \text{Fe}^{3+}$ hopping frequency and thus, dipoles lining up parallelly toward the field direction amplifies the loss. Whereas at higher frequencies the growth of resistive layer by interfacial polarization as well as the delaying of polarization may have jointly led to a drop in $\tan \delta$ [63, 64]. As it is clear from Fig. 6c that 20% Co doped sample possesses the lowest dielectric loss compared to other composites. If the resistive layer is thin enough then, less energy will be required for jumping in Fe^{3+} and Zn^{2+} grains and this may reduce $\tan \delta$. Hence, for intensifying the skin depth, low dielectric losses are essential to facilitate the microwaves' flow through the bulk of ferrite materials [65]. With the further increment of frequency, we observe a tendency of elevation in $\tan \delta$ for undoped and 10% Co substituted samples. This augmentation is due to the presence of relaxation function that makes $\tan \delta$ to dominate more in higher frequency ranges. Moreover, under the pressure of applied field, grains adjacent to the grain boundaries produce a localized charge aggregation, which confirms that the space charge polarization are present in materials [57, 66].

3.3 Conductivity

As well recognized magnetic substance, ferrites possess lower conductivity and thus, they have wide applications at microwave frequencies [67]. For understanding the conduction mechanism,

frequency-dependent AC conductivity (σ_{AC}) was analyzed at RT for all the sintered $\text{Ni}_{0.6}\text{Zn}_{0.4-x}\text{Co}_x\text{Fe}_2\text{O}_4$ ($0 \leq x \leq 0.2$) ferrites. The σ_{AC} values were determined using the formula as $\sigma_{AC} = \omega \epsilon_0 \epsilon' \tan \delta_E$; here ϵ_0 and ω being the permittivity of free space and radial frequency, correspondingly.

As we can detect from Fig. 7a, the variation of σ_{AC} with frequency shows two separate regions: one is the plateau region at lower frequencies where the conductivity of all the samples except $x = 0.00$ remains almost steady, and another one is the dispersive region at high frequencies where the conductivity rises more rapidly. Usually, if conductivity is caused by the hopping of charges, σ_{AC} will increase with frequency, and if the band conduction is used, σ_{AC} will decrease [68]. The AC conductivity observed in this study satisfies Jonscher's power law: $\sigma_{AC}(\omega) = \sigma_{DC}(\omega = 0) + A\sigma\omega^s$, where the factor A depends on temperature and 's' ($0 \leq s \leq 1$) is a dimensionless exponent [69]. Whereas frequency independent DC conduction (σ_{DC}) (when $s = 0$) is attributed to the hopping transition and this induces the electrical transportation that is longer in range as well as in time limit [111] [70].

Free charges in dielectric ferrites are almost nonexistent for conduction mechanism. As reported by Koop's phenomenological theory [71] of conductive behavior and Maxwell–Wagner [72, 73] modeling, grain boundaries play a greater functioning role

compared to grains at lower fields, which obstructs the charge carriers' mobility. Furthermore, Verwey de Boer mechanism suggested that with heightened applied field, the resilient grain boundary shows foremost impact on the lower side of the field. Thus, it boosts the interchange of electrons at B-sites between Fe^{2+} and Fe^{3+} n-type ions [74] that raises σ_{AC} . Besides, on [B] site, the hopping of holes can also be introduced among Ni^{2+} and Ni^{3+} p-type ions as in the form of inverse spinel structure Ni-Zn ferrites, which further adds to the electrical conductivity [75]. Considering the small conductivity (as observed in Fig. 7a) at RT of the sintered NZFO and Co-doped NZCFO ferrites, hopping of electron ($\text{Fe}^{2+} \leftrightarrow \text{Fe}^{3+} + e^-$) is stronger in contrast of hole leaping ($\text{Ni}^{3+} \leftrightarrow \text{Ni}^{2+} + e^+$) and so, the conduction mechanism is mostly tuned by n-types [76]. It is also visible that with the increasing Co content (except for $x = 0.10$ content) σ_{AC} decreases. This can be ascribed because of the enlarged hopping length amongst the A- and B- sites' ions which reduces the movability of electric charges. Besides, the development of several oxidation states increases the probability of cations accumulation, and this can reduce the electron conductivity [77]. The slope from $\log(\sigma_{AC})$ vs. $\log(f)$ curves (Fig. 7b) specify 's' exponents (defined in Jonscher's principle) that are presented in Table 2. The curves reveal a nearly straight line for all the studied composites from 3×10^4

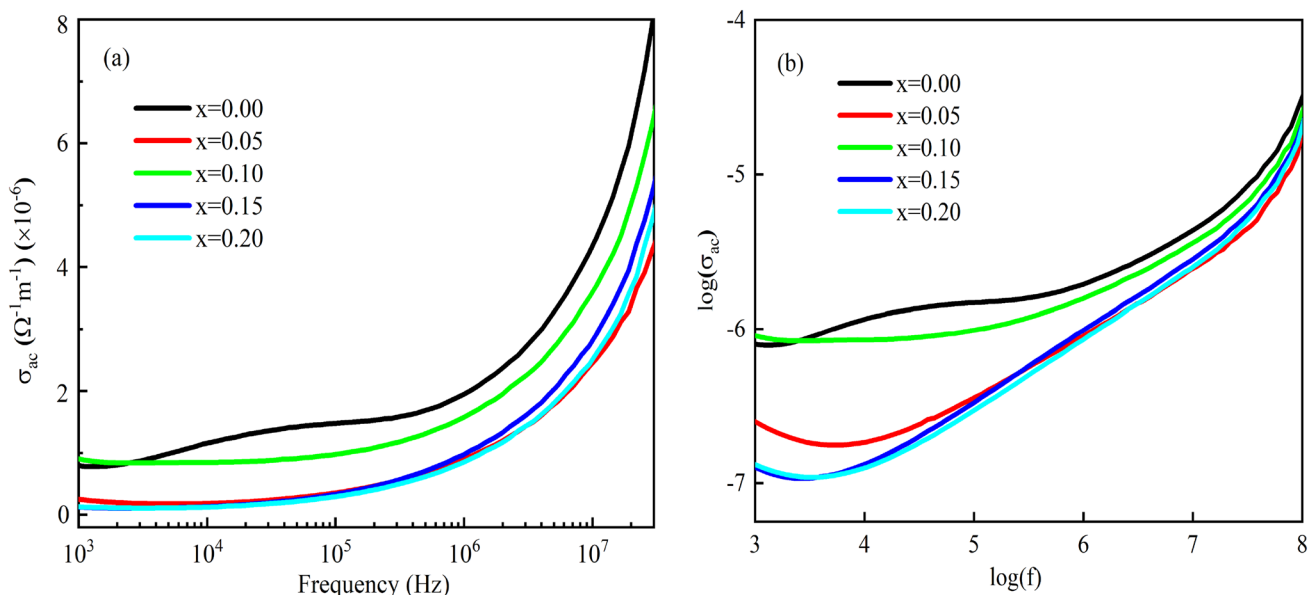


Fig. 7 **a** The conductivity (σ_{AC}) deviation and **b** logarithmic change of σ_{AC} with respect to frequency for $\text{Ni}_{0.6}\text{Zn}_{0.4-x}\text{Co}_x\text{Fe}_2\text{O}_4$ ferrites ($0 \leq x \leq 0.2$) at RT

Hz to 1MHz frequency ranges. Furthermore, one may notice from Table 2 that with 5% Co substitution, the 's' factor increases from 0.3 to 0.46 but then decreases for 10% Co addition and finally increases again up to 0.51 for the further Co addition. The attained values of 's' recommend that the conducting process in the experimented composites pursue the hopping mechanism. This also implies that mobility of carriers dominates the conductivity of considered samples not the concentration of charges.

3.4 Impedance measurements

The Cole–Cole or Nyquist scheme (AC impedance spectrum) is widely used as an effective technique for determining the correlation of electrical properties and microstructures of ferrites. For polycrystalline composites, analyzing complex impedance ($Z^* = Z' + jZ''$) with resistive (Z' , real part) and reactive (Z'' , imaginary part) contribution is helpful for separating the grain and grain-boundary impacts on the total conductivity in the broader range of frequency spectrum. Figure 8a, b display the frequency deviancy of Z' and Z'' for $Ni_{0.6}Zn_{0.4-x}Co_xFe_2O_4$ ($0 \leq x \leq 0.2$) compositions. As Z' for all specimens are significantly large near low frequency zone, specifying the polarization is extreme. This indicates that even if the measurement frequency is very low, relaxation is not taking place for grain boundaries. The sharp decrease of Z' with the increasing frequency confirms the amplified AC conductivity in the NZCFO composites. At further higher ($> 10^5$ Hz) frequency domain, the merging of Z' and the plateau-like behavior implies that at homogeneous phase boundaries, the external field may have influenced the freeing of space charge aggregation in synthesized materials and a consequential dropping of properties of energy barrier [78, 79]. The space charges, at higher frequencies, can relax for a shorter period which quickens their recombination [80] and therefore, leads to a merging of curves for all the compositions. Among the five composites under scrutiny, 5%, 15% and 20% Co doped samples are showing significantly improved impedance at low frequencies. This outcome agrees quite well with the observed conductivity results (as detected in Fig. 7a), which indicated that these specified composites have the highest values of conductivity than the undoped and 10% Co doped samples.

Some key features are observed in Fig. 8b: (i) the emergence of a familiar relaxation peak which is broad in nature for all the specimens at lower frequency

Table 2 The variation of frequency exponent factor (s), relaxation time (τ),full width at half maxima(β), saturation (M_s) and remanent (M_r) magnetization, coercive field (H_c), magnetic moment (n_B), anisotropy constant (K), Yaffet-Kittel angle (α_{Y-K}), static permeability, resonance frequency(f_r), relative quality factor (RQF) parameters with Co concentration in Ni-Zn ferrites

Composition	s-factor	τ (μ s)	B	M_s (emu/g)	M_r (emu/g)	H_c (Oe)	n_B (μ_B)	K (erg/g)	α_{Y-K} (deg)	Static μ'_i at f_r (MHz)	μ'_i at		RQF _{max}		
											$\mu'_i \times f_r$ (GHz)	10^3 Hz		100 MHz	
x=0.00	0.30	0.50	0.019	69.43	2.04	15.18	2.95	1098.12	15	61.80	78.52	4.85	242.45	68.80	4371.50
x=0.05	0.46	2.75	0.010	60.68	1.10	21.20	2.57	1340.18	33	24.85	120	2.98	428.85	44.03	1837.77
x=0.10	0.33	0.89	0.018	67.77	2.31	20.25	2.87	1429.30	35	50.17	90.44	4.54	393.75	69.91	3943.43
x=0.15	0.51	3.16	0.013	87.39	1.42	22.46	3.69	2044.22	31	16.54	120	1.98	397.14	2.78	1265.50
x=0.20	0.51	4.19	0.012	80.65	0.27	4.40	3.40	369.67	41	11.26	120	1.35	418.26	0.76	683.85

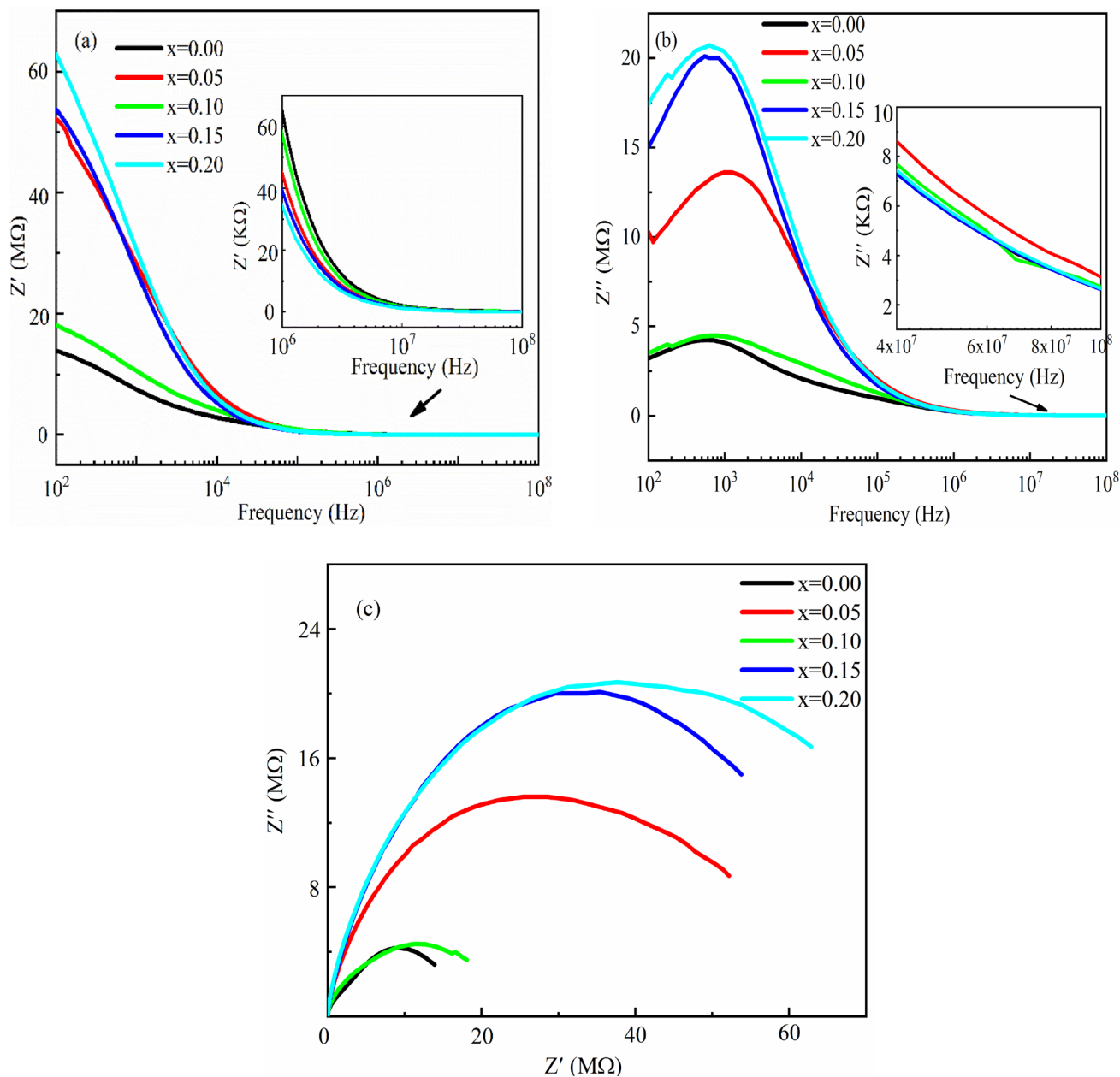


Fig. 8 Complex impedance spectrums: **a** real part and **b** imaginary part against frequency and **c** Nyquist plot of $\text{Ni}_{0.6}\text{Zn}_{0.4-x}\text{Co}_x\text{Fe}_2\text{O}_4$ ($0 \leq x \leq 0.2$) ferrites

region (from 10^2 – 10^5 Hz); (ii) the gradual diminution of Z'' to a lowest value with the expanding frequency and finally a tendency of merging of Z'' values at further higher frequencies; (iii) the attenuation in the absolute Z'' value with an explicit shift of the peaks toward expanded frequencies for undoped and 10% Co doped composites. Very similar behavior was observed in Ref. [21], which suggested that the reduction of Z'' is possibly caused by the existence of oxygen voids or

space charge relaxation of immobile charges at grain boundaries. Furthermore, at large frequencies, all the merging trajectories implies a depletion to the space charge polarization with expanding frequency [81]. To understand the electrical mechanism going on within the ferrite materials even better, the Nyquist plots for $\text{Ni}_{0.6}\text{Zn}_{0.4-x}\text{Co}_x\text{Fe}_2\text{O}_4$ composites are depicted in Fig. 8c. Here, the data analysis was carried out by plotting $Z'' (= |Z| \sin \theta = -\frac{1}{\omega C})$ against $Z' (= |Z| \cos \theta = R)$

on a complex plane; where θ is the phase difference of voltage and current and $|Z|$ can be calculated as $Z = \sqrt{Z'^2 + Z''^2}$. By Brick layer model, the impedance for an RC parallel circuit (counterpart of impedance plot) is conveyed as:

$$Z' + jZ'' = R/(1 + j\omega RC) \tag{8}$$

A more simplified expression is,

$$\left(Z' - \frac{R}{2}\right)^2 + Z''^2 = \left(\frac{R}{2}\right)^2 \tag{9}$$

Comparing Eq. (9) with standard circle formulation, the Nyquist plot is a semicircle in the first quadrant with a radius of $\frac{R}{2}$ and with a center at $(\frac{R}{2}, 0)$. In typical Cole–Cole plots, two semicircles overlap. However, as perceived in Fig. 8c, we have detected only one incomplete semicircle for undoped and all the Co doped compositions. This observation indicates that grain boundary greatly affects the conducting mechanism for these specimens, whereas the grains' contribution cannot be determined [44]. This may have been caused owing to the limited frequency (10^2 – 10^8 Hz) dimension used in the present study, which wasn't enough to separate the influence of grain boundary from the grain contribution [82]. Furthermore, the semicircle centers for all composites are observed beneath the real impedance axis, which for dielectric materials is a distinguished characteristic and known as non-Debye type relaxation. Moreover, the close examination of Cole–Cole plots demonstrates that compared to the undoped sample, the arc diameter increases with the addition of Co doping except for $x = 0.10$. The enlarging tendency of arc diameter for NZCFO ferrite materials signifies that the grain resistances may have diminished with Co addition.

3.5 Electric modulus investigation

Studying electric modulus spectrum is important for ascertaining the relaxation mechanism of applied field due to the bouncing of charges inside electron/ion-conducting matters when the effects of low frequency electrode polarization are restricted [74, 83]. To inspect the relaxation characteristics, functionality of electric modulus for various ceramic compositions [84, 85] have been studied previously with the following expressions [86]:

$$M^* = M' + iM'' = M_\infty \times \left[1 - \int_0^\infty dt + \exp(-\omega t) \left(-\frac{d\phi}{dt}\right) dt\right] \tag{10}$$

where, $\phi(t) = \exp[-(t/\tau)]$ symbolizes the evolution of time of electric field inside the dielectrics, τ denotes the conductivity relaxation time; while β implies the range of non-Debye characteristic that is associated with FWHM of the imaginary (M'') curves [74]. Here, M' and M'' parts are calculated as follows:

$$M' = \frac{\epsilon'}{\epsilon'^2 + \epsilon''^2} \tag{11}$$

$$M'' = \frac{\epsilon''}{\epsilon'^2 + \epsilon''^2} \tag{12}$$

Figure 9a, b demonstrate the alternation of M' and M'' trajectories for NZCFO composites with expanding frequency. According to Fig. 9a, $M'(\omega)$ for all the samples is very smaller (approaching to zero) at lower frequencies ($< 10^3$ Hz). Whereas with the increasing frequency, $M'(\omega)$ initially shows a rapid growth and finally illustrates a saturation like behavior at maximum asymptotic value (i.e., $M_\infty = 1/\epsilon_\infty$). This phenomenon implies a short-range portability of the charge carriers' conduction mechanism in the synthesized materials [87]. The smaller M' values at lower frequencies, assists the conduction process because of the charge carriers' long-range mobility and owing to a negligible contribution of electrode polarization in ferrites [88]. On the other hand, at elevated frequencies, due to the lower mobility, holes will have a smaller contribution compared to that of electrons. Therefore, the exchange of holes among Ni^{2+} and Ni^{3+} ions may locally cause dislocations in the reversed applied field direction, whereas the exchanging of electrons among Fe^{2+} and Fe^{3+} ions is directionally parallel, and these are maybe the sources of dielectric polarization inside Ni–Zn–Co ferrites [89].

The $M''(\omega)$ spectrum corresponding to different Co concentrations is characterized by the presence of asymmetrical peaks that are centered around the dispersion area of $M''(\omega)$ (as presented in Fig. 9b) revealing an extreme conduction loss. Apart from the 10% Co doped sample, the peaks with increased Co concentration move towards the lower frequency region in comparison to the undoped one. The low-frequency side of $M''_{max}(\omega)$ (i.e., left portion of the peak) is referring to long-range portability of charge carriers that could move over widened spaces, which

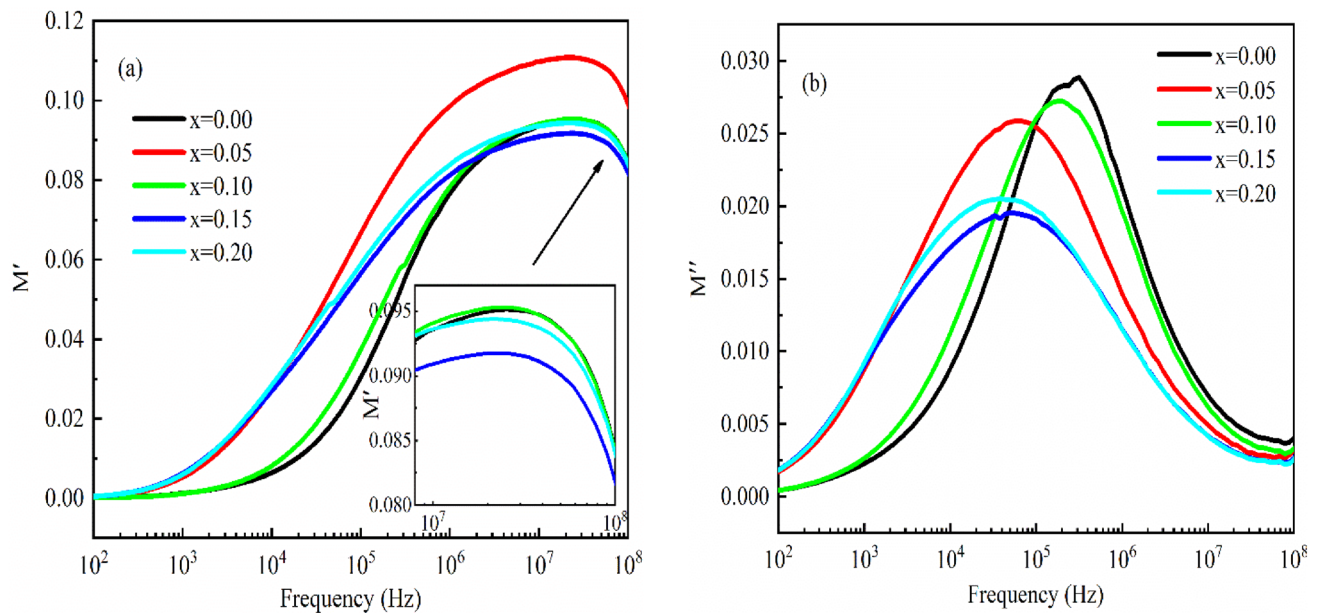


Fig. 9 **a** Real and **b** imaginary parts of complex electric modulus against frequency for Ni–Zn–Co composites

means they can effectively jump between the adjacent sites within this frequency limit [74]. In contrast, the peak's right position (i.e., at extensive frequency ranges) is attributed to carriers that can conduct the localized movements only because of the confinement in narrow potential wells (short-range mobility) [90]. Relaxation time $\tau = 1/2\pi f_{max}$ for NZCFO samples are presented in Table 2, where maximum $M''(\omega)$ point determines the characteristic frequency f_{max} (denoted as M''_{max}). For all the studied samples, τ values are within the microsecond range, and for 20% Co doped content, we have obtained the maximum value of 4.19 μ s. Sometimes, high sintering temperature can make the grain boundary move faster, resulting in an easy relaxation of dielectric spin, and because of the quantum size effect, the spin-relaxation times can be strongly enhanced and reach to μ s range, which is extended in magnitude compared to other bulk systems or conventional metallic thin films [91].

Figure 10a exhibits the normalized plot of M''/M''_{max} vs. f/f_{max} for NZCFO composites. The observed wide-ranging peak is due to the summing-up of relaxations taking place within the bulk ferrite materials. As it is known that $\beta \rightarrow 1$ (stretched parameter) corresponds to the ideal Debye type relaxation and $\beta \rightarrow 0$ implies the highest interaction among the ions [92]. The β , i.e., full width at half

maxima values obtained (as shown in Table 2) for all the compositions are very lower, which suggests that there exists a strong ion–ion interaction that magnifies the relaxation disparity relative to the Debye relaxation mode. Figure 10b depicts the distinguishability of M'' and Z'' with respect to frequency for 15% Co doped composition. For ideal Debye type relaxation, at a particular frequency, the two peaks would have overlapped with each other. But in our present case, the two peaks are significantly separated which again confirms the departure from standard Debye-type behavior.

Figure 10c represents M'' vs. M' spectrum of NZCFO ferrites. It was previously reported that the presence of two semicircles (that are well resolved) is the common characteristic in electric modulus spectra [54, 93]. In this investigation, one semicircular arc visibly appears for all the samples implying that the relaxation arises only on account of the influence of grain boundary, while the contribution of grains is repressed. Moreover, it is noteworthy to mention that the beginning of all the semicircles doesn't coexist at the origin, which specifies that there may exist other relaxation processes at lower frequencies for the synthesized ferrites. For undoped and Co doped materials, the arc center beneath the real axis specifies a development of non-Debye relaxing process, which supports our earlier conclusions.

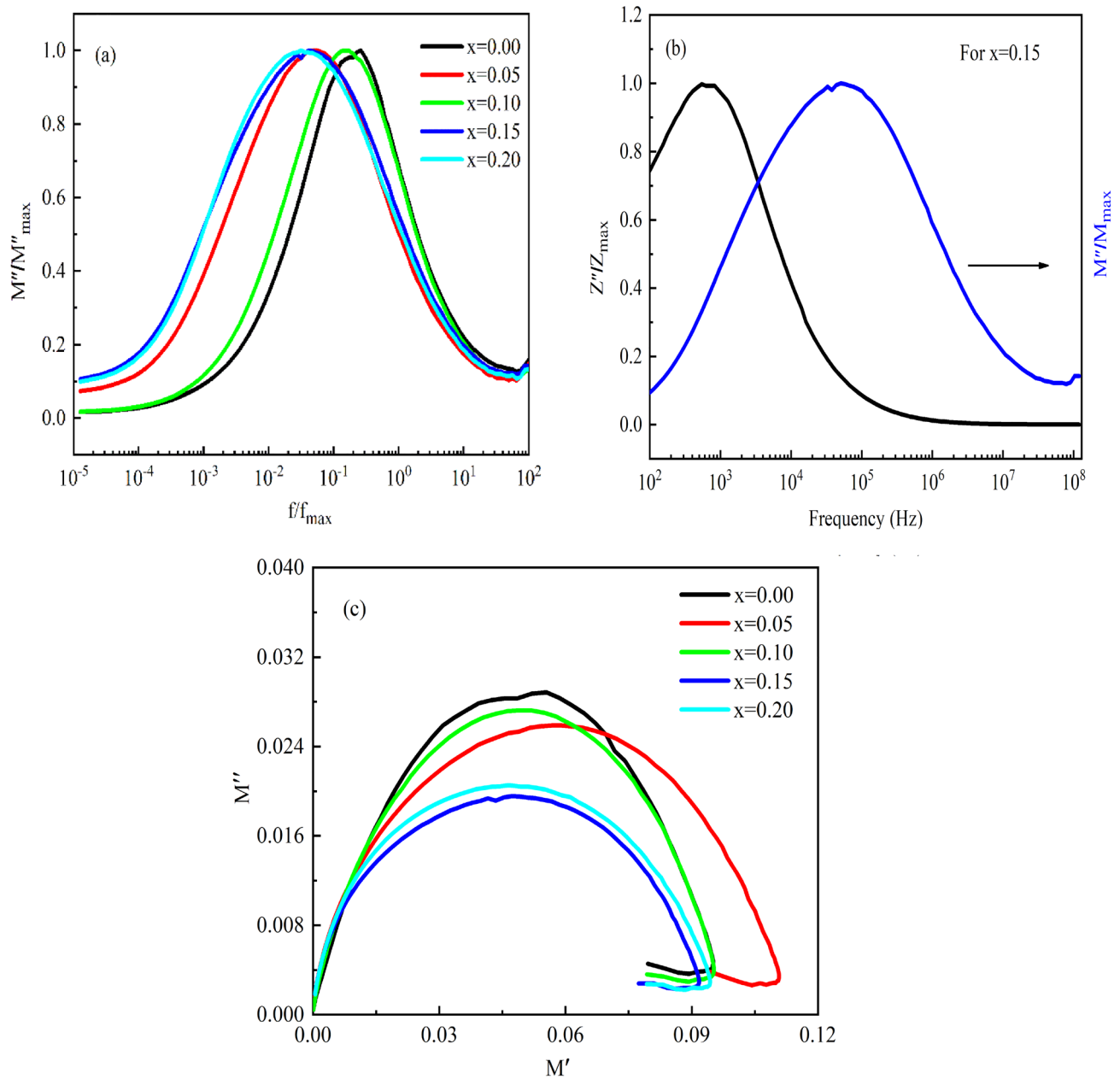


Fig. 10 **a** Normalized parameters (M''/M''_{max}) against $\log(f/f_{max})$ for different concentrations of Co, **b** the alteration of Z'' and M'' against frequency for 15% Co doped Ni-Zn ferrite and **c** complex modulus spectrum of NZCFO specimens

Moreover, as observed in Fig. 10c, the appearance of M'' vs. M' spectrum and the arc radius have varied with Co substitution, which indicates that there is a probable alteration in the capacitance values relative to Co content.

3.6 Magnetic characterization

In order to analyze the dynamic hysteresis loop for unfolding the magnetic performance of NZCFO at RT, M - H loops up to 20 kOe maximized field were studied and depicted in Fig. 11. The loops reveal that magnetization increases for all the compositions as the applied field is intensified and eventually attains its

static saturation, which is an evident of soft magnetic substances. The magnetic measurements (from the hysteresis curves), e.g., saturation (M_s) and remanent (M_r) magnetization as well as coercivity (H_c) are exhibited in Table 2. Furthermore, using M_s quantities, magnetic moment $n_B = \frac{M_w \times M_s}{5585}$ (M_w =molecular weight of compositions) in Bohr magneton were also determined. For all specimens, the K (=anisotropy constant) values were also computed from the expression: $H_c = \frac{0.96 \times K}{M_s}$. Table 2 distinctly shows that with the initial 5% Co doping, saturation magnetization descends compared to undoped composition but afterwards, for 10% and 15% Co substituted specimens, M_s values have significantly enhanced, and finally, it again declines with the further adding of Co ($x=0.20$). According to the site occupancy preference, we have proposed above that Zn^{2+} ions in Ni-Zn ferrites inhabit A- sites and Ni^{2+} ions prefer B- sites, whereas both sites can be occupied by Fe^{3+} ions. Since the respective magnetic moments of Fe^{3+} , Ni^{2+} and Zn^{2+} ions are 5, 2 and 0 μ_B , hence in Ni-Zn ferrites, n_B of tetrahedral sites is lower contrary to the octahedral sites [42]. Alternatively, Co has a tendency of occupying both sites; so, when Co with 5% concentration is doped in NZFO, most of the Co^{2+} ions take place B-site rather than site A [94, 95]. Once Co^{2+} ions with its higher magnetic moment (3 μ_B) start to inhabit (A) site, Zn^{2+} ions get displaced from (A) to [B] position. This may cause a significant drop of n_B along with its magnetic saturation (previously

revealed in Table 2). Whereas, with increasing Co ($x=0.1, 0.15$) concentrations, more Co^{2+} ions substitute Zn^{2+} ions at A- sites and consequently, larger M_s values are obtained. A similar result in magnetization has been observed with the changing Co concentration in $Ni_{0.6-x}Zn_{0.4}Co_xFe_2O_4$ ferrites [23].

Lastly, according to Yaffet and Kittel, the diminution of magnetization with the further Co addition beyond $x=0.15$ may have happened because of the presence of noncollinear spin configuration. NZCFO ferrites with 20% Co addition, may show the spin canting effect which improves Yaffet-Kittel (α_{Y-K}) angle. Here, for all the NZCFO compositions, the α_{Y-K} values were estimated applying the formula $n_B = M_B(x)\cos\alpha_{Y-K} - M_A(x)$, and are displayed in Table 2. Evidently α_{Y-K} angles are nonzero, while the lowest one is obtained for undoped sample and highest for $x=0.20$ composition. The enhancement in α_{Y-K} values for 5%, 10% and 20% Co doped samples suggest that the previously considered strong A-B interaction has weakened in octahedral sites. The declining of A-B interaction in Ni-Zn ferrites may have happened because of the A- site preference of substituted Co^{2+} ions with high concentration. This makes the A-A interaction strongly interpret spins that parallelly oriented at octahedral site and therefore, the ordering doesn't remain collinear [96]. Moreover, the inconsistency in the observed M_s values may have formed due to the abruptly changed lattice parameters with enhanced Co contents.

On the other hand, the remanent magnetization declines with 5% Co substitution, which later increases remarkably for 10% Co doped composition, but it again visibly starts to decline for the further Co addition. However, the H_c value of the acquired 5% Co doped ferrite has boosted dramatically with respect to undoped one, then after decreasing slightly for $x=0.10$ it rises significantly for 15% Co doped composition which again gets diminished as more Co is substituted. It was reported that coercivity of ferrites will be higher when the grains are smaller in size, and the porosity is larger [97]. Thus, for 5% and 15% Co doped ferrites, the diminished grain size and the augmented porosity maybe the reasons of increased H_c values. Whereas the decrement in H_c with more addition of Co ($x=0.20$) is expected because of the presence of a larger number of grains (as previously observed from the SEM micrographs) which contain a larger volume of domain walls. With an expanded grain size, the domain walls' number grows, and their movement

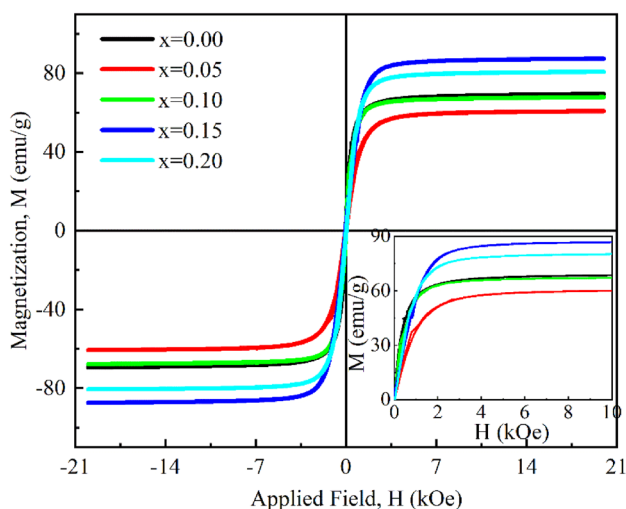


Fig. 11 The variation of M - H loops of $Ni_{0.6}Zn_{0.4-x}Co_xFe_2O_4$ ($0 \leq x \leq 0.2$) ferrites at RT

contributes a lot to magnetization without spending much energy compared to the domain rotation [98, 99]. Besides, magnetocrystalline anisotropy which generally gets induced by lattice distortion [31] can be varied by cation distribution in the ferrite systems and this may affect the coercivity. Table 2 also shows that anisotropy constant (K) values of Ni–Zn ferrites have increased with Co addition up to 15%. This points out that the 111 direction i.e., easy axis magnetization is not parallel to the fixed direction which may induce magnetic poles near the grain boundaries. Larger K values in Co doped samples indicate that the domains have accumulated within the grains of ferrites which causes a dispersion of magnetic poles and therefore, enhances the magnetocrystalline anisotropy energy [100]. Whereas, for 20% co-doped sample K has significantly diminished to 369.67 erg/g. As previously mentioned, this specific composition has also shown a huge reduction in coercivity. This outcome may have been influenced by the weakening of spin-orbit coupling which differs with the congregation of A-sited Zn^{2+} and A/B-situated Co^{2+} ions.

3.7 Permeability analysis

Complex initial permeability ($\mu_i^* = \mu_i' - j\mu_i''$) vs. frequency schematic for NZCFO specimens are portrayed in Fig. 12a, b. Where, μ_i' (real part) designates the restrained energy as it exhibits magnetization relative to the changing magnetic field, and μ_i'' (imaginary portion) specifies the energy that is dissipated by manifesting B phasing-out with H [57]. As a microstructural function, μ_i^* depends strongly on processing parameters such as composition, stoichiometry, impurity concentration, crystal anisotropy and magnetostriction. It is observed in Fig. 12a, μ_i' for all the specimens exhibit typical curves that remain nearly constant below 10^7 Hz frequency range. Afterwards, it increases a bit up to a maximum point signifying the existence of resonance and afterwards around high frequencies, it goes down rather promptly to the lowest point, which agrees with the Globus model [101]. This continuous phenomenon of μ_i' throughout the wider frequency area specifies the compositional steadiness as well as the attribute of NZCFO ferrites formulated using double sintering technique. As for the imaginary part of complex permeability, Fig. 12b distinctly shows that μ_i'' decreases sharply up to $\leq 10^5$ Hz. Then after remaining

constant over a certain frequency range, it starts to rise with the increasing frequency and finally an apparent peak appears at a certain frequency for NZFO, 5% and 10% Co substituted NZCFO compositions, which is an evident of ferrimagnetic resonance.

Table 2 presents the evolution of permeability in Ni–Zn–Co composites. The diminution of the static initial permeability as well as the $\mu_i' \times f_r$ (f_r denotes the resonance frequency determined from the highest point of μ_i'' at high-frequency region) factor with cobalt incorporation ($x = 0.05, 0.15$ and 0.20) was spotted, which then unusually elevated for $x = 0.10$. Moreover, Fig. 12a clearly demonstrates that the spectra become sharper for 5% and 10% Co doped compositions compared to the undoped one. At lower frequencies, permeability of ferrites comes mainly from domain wall displacements, and at higher frequencies, it arises from the rotational resonance (spin resonance) [102]. A previous report explains that Co constrains the domain walls' movement [103] and this initiates two effects: (i) the depletion of permeabilities with Co substitution and (ii) the stimulation of spin rotation with Co substitution by transporting the resonance frequency toward higher applied field. However, the improvement in μ_i' for 10% Co doped Ni–Zn ferrite may be ascribed because of: (i) enhanced bulk density and reduced grain size (previously detected from XRD and SEM inspection) and (ii) diminished magnetocrystalline anisotropy constant, which may have resulted by the diminution of crystal anisotropy as well as inward stress [104]. Sometimes, a little addition of cobalt can recompense negative magnetocrystalline anisotropy in the host crystal (Ni–Zn ferrites) on account of its large positive magnetocrystalline anisotropy [105]. This might cause a minimum hindrance to the motion of domain walls and, therefore, makes 10% Co doped Ni–Zn ferrite a comparatively significant material for high frequency potential devices.

The frequency variation of magnetic loss, $\tan\delta_M (= \frac{\mu_i''}{\mu_i'})$ for $\text{Ni}_{0.6}\text{Zn}_{0.4-x}\text{Co}_x\text{Fe}_2\text{O}_4$ compositions was also studied and displayed in Fig. 12c. It should be specified that the domain walls begin to show lag in following the field if there are imperfections in the lattice, which can initiate loss [57]. A dispersion in $\tan\delta_M$ for undoped and Co doped samples is observed initially at low range ($\leq 10^5$ Hz) frequencies which later behaves almost independently up to 10^7 Hz frequency. Besides, from the corresponding figure,

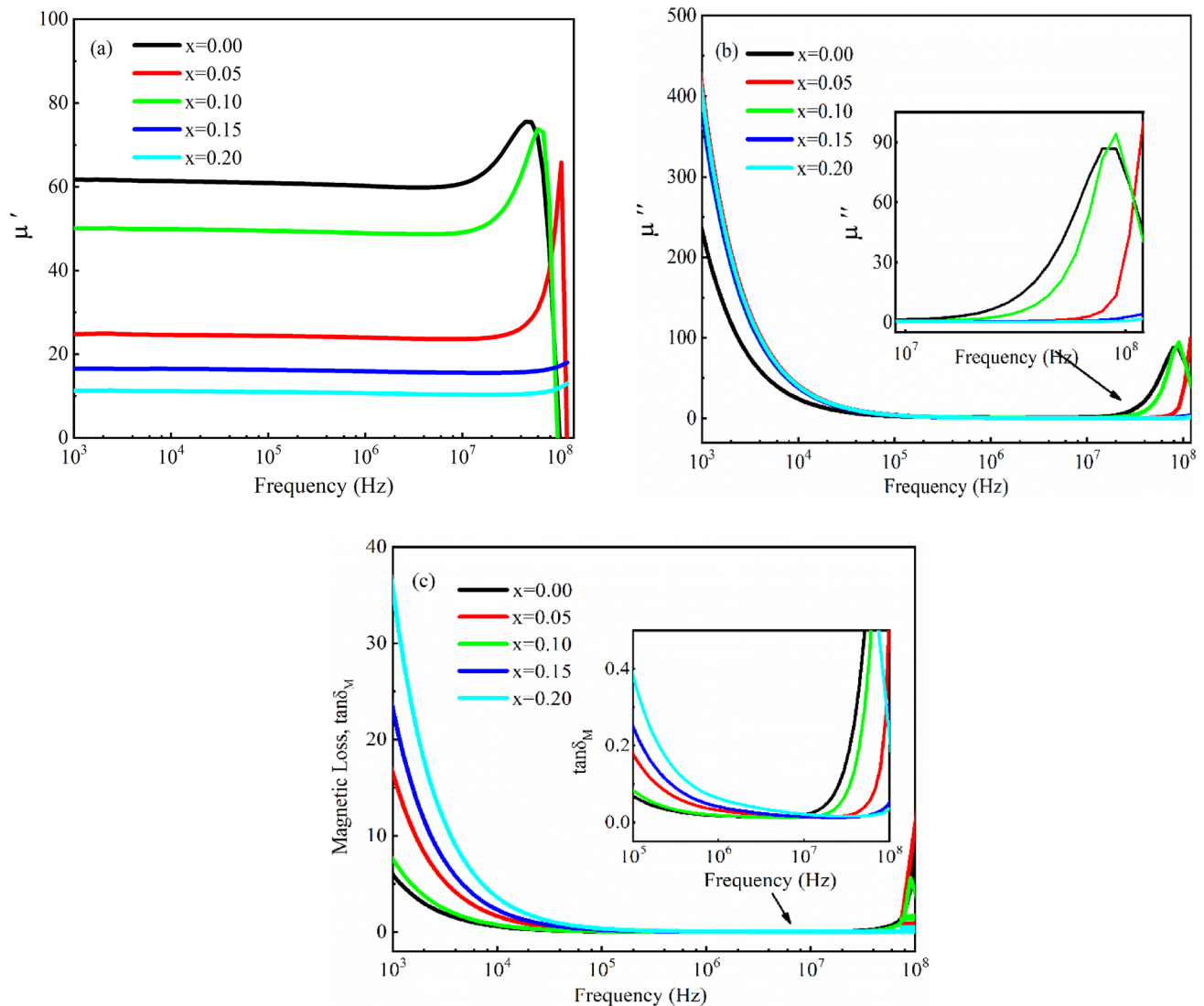


Fig. 12 **a** Real part, μ'_i and **b** imaginary part, μ''_i of initial permeability and **c** magnetic loss factor ($\tan\delta_M$) with respect to frequency for $\text{Ni}_{0.6}\text{Zn}_{0.4-x}\text{Co}_x\text{Fe}_2\text{O}_4$ ($0 \leq x \leq 0.2$) compositions

it is distinctly noticeable that although the values of $\tan\delta_M$ are higher for Co doped samples compared to the undoped one, for 10% Co doped composition, the magnetic loss gets reduced significantly. However, at further higher frequencies ($> 10^7$ Hz), a sudden increase in $\tan\delta_M$ is detected in all the compositions. Since, at some point, the phase lagging between the applied field and domain rotation becomes greater than the domain wall movement, domain rotation starts to dominate more than domain wall movement, which induces magnetic loss at a higher frequency region. This phenomenon makes the synthesized NZCFO materials more efficient over a

broad range of frequencies that are suitable for MLCI applications.

For all the synthesized NZCFO compositions, the changes of relative quality factor, $\text{RQF} = \frac{\mu'_i}{\tan\delta_M}$ (which determines the quality or performance of a magnetic material) with respect to frequency are presented in Fig. 13. RQF for undoped and Co doped composites elevates dramatically with increased frequency, then after showing a widely spread peak, it starts to descend rapidly with the further increment of frequency. Moreover, it is clearly distinguishable that although with the enhancement of Co content, RQF declines, it has improved significantly for 10% Co

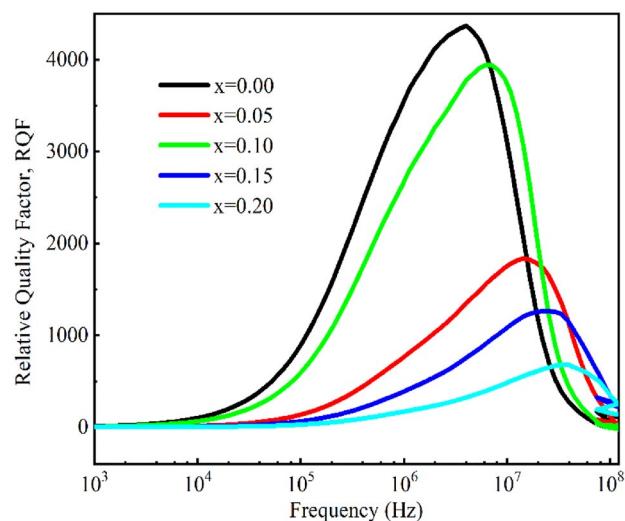


Fig. 13 Frequency variation of RQF for Co doped $\text{Ni}_{0.6}\text{Zn}_{0.4-x}\text{Co}_x\text{Fe}_2\text{O}_4$ ($0 \leq x \leq 0.2$) ferrites

doped composition. Besides, in comparison to the undoped one, peak positions of NZCFO get shifted toward high frequencies. This occurrence of diminution in RQF values is associated with Snoek's law, which states that the augmentation of saturation magnetization can cause a depletion in resonance frequency and vice versa. Table 2 displays the maximum RQF values for different compositions, which reveals that the highest RQF was obtained for undoped Ni-Zn ferrite sample, while the lowermost loss tangent value (according to Fig. 12c) was also detected for this composition. This is presumably due to the presence of homogeneous and small grained microstructure, larger bulk density, less defects, and fewer imperfections in comparison to the other Co substituted specimens. Whereas the deterioration of RQF in Co doped samples may have been caused due to the quick progress of grains as larger ones normally result in low RQF.

4 Conclusions

A thorough investigation on structural, electrical (AC impedance, and modulus spectroscopy) and magnetic (initial permeability and M - H loops) characteristics of $\text{Ni}_{0.6}\text{Zn}_{0.4-x}\text{Co}_x\text{Fe}_2\text{O}_4$ ($0 \leq x \leq 0.2$) ferrites is presented in this paper. XRD and FTIR spectrums confirm a cubic single-phase

formation. Crystallite size estimated using W-H method was found in the range of 68–110 nm. The variation detected in the experimentally calculated lattice parameter is in close conformity with the theoretically computed one, i.e., satisfying the suggested cation sharing. NZFO has shown the highest AC conductivity but a noteworthy increase in σ_{AC} is observed for 10% Co doped composition in comparison to the rest. Cole–Cole plots have demonstrated an enlarging tendency of arc diameter for 5%, 15% and 20% NZCFO ferrite materials. A significant enhancement in M_s (87.39 emu/g) and in anisotropy constant (2044.22 erg/g) have been noticed for 15% Co concentration. The diminished grain size and the rise in porosity in 5–15% Co doped ferrites may have increased their H_c values (21.20, 20.25 and 22.46 Oe respectively). The permeability curves have displayed sharp peaks at high frequencies ($> 10^7$ Hz) for undoped and 5–10% Co substituted NZCFO compositions. Measured higher RQF's of the synthesized NZCFO ferrites make them compatible for high-frequency functional devices.

Acknowledgements

The authors express their heart-felt gratitude to the Materials Science Division, Atomic Energy Centre, Dhaka, for extending the use of experimental facilities. We also acknowledge the Centre for Advanced Research in Sciences (CARS), University of Dhaka and Nano and Advanced Materials Laboratory, Department of Physics, University of Dhaka, for their co-operation while carrying out this research. The authors would also like to thank the Bose Centre for Advanced Study and Research in Natural Science, University of Dhaka, for supporting this work.

Author contribution

Authors MNIK, USA and AA contributed to the study of conception and design. Material preparation and data collection and analysis were performed by USA, AA, KHM, MKA and AK. The first draft of the manuscript was written by AA and KHMaria. All authors commented on the previous version of the manuscript and after reading it they have approved the final manuscript.

Funding

One of the authors (U. S. Akther) got partial financial support (fellowship) from Bose Centre for Advanced Study and Research in Natural Science, University of Dhaka.

Data availability

The datasets collected and analyzed during the current study are available from the corresponding author on reasonable request.

Declarations

Competing interests The authors have no competing interests to declare that are relevant to the content of this article.

Ethical approval There was no potential conflict of interest between the authors and this research topic. This research doesn't involve any human participants and/or animals. Informed consent is not applicable as no human or animal subjects were involved in this research.

References

1. M. Sorescu, L. Diamandescu, R. Peelamedu, R. Roy, P. Yadoji, *J. Magn. Magn. Mater.* **279**, 195 (2004)
2. J.T.S. Irvine, A. Huanosta, R. Valenzuela, A.R. West, *J. Am. Ceram. Soc.* **73**, 729 (1990)
3. B.P. Rao, K.H. Rao, *J. Mater. Sci.* **32**, 6049 (1997)
4. S. Aman, N. Ahmad, B.S. Almutairi, M.B. Tahir, H.E. Ali, *J. Electron. Mater.* **52**, 4149 (2023)
5. S. Aman, S. Gouadria, F.F. Alharbi, M.N. Saeed, H.M.T. Farid, *Appl. Phys. A* **129**, 347 (2023)
6. M. Arshed, M. Siddique, M. Anwar-ul-Islam, N.M. Butt, T. Abbas, M. Ahmed, *Solid State Commun.* **93**, 599 (1995)
7. S.F. Wang, Y.F. Hsu, K.M. Chou, J.T. Tsai, *J. Magn. Magn. Mater.* **374**, 402 (2015)
8. A. Verma, O.P. Thakur, C. Prakash, T.C. Goel, R.G. Mendiratta, *Mat. Sci. Eng. B* **116**, 1 (2005)
9. J. Gutiérrez-López, B. Levenfeld, A. Várez, J.Y. Pastor, I. Cañadas, J. Rodríguez, *Ceram. Int.* **41**, 6534 (2015)
10. M.M. Haque, K.H. Maria, S. Choudhury, M.A. Bhuiyan, M.A. Hakim, *J. Ceram. Process. Res.* **14**, 82 (2013)
11. K.H. Maria, S. Choudhury, M.A. Hakim, *Int. Nano Lett.* **3**, 42 (2013)
12. M.A. Hakim, S.K. Nath, S.S. Sikder, K.H. Maria, *J. Phys. Chem. Solids* **74**, 1316 (2013)
13. S. Noor, M.A. Hakim, S.S. Sikder, S.M. Hoque, K.H. Maria, P. Nordblad, *J. Phys. Chem. Solids* **73**, 227 (2012)
14. S.K. Nath, K.H. Maria, S. Noor, S.S. Sikder, S.M. Hoque, M.A. Hakim, *J. Magn. Magn. Mater.* **324**, 2116 (2012)
15. J. Gutiérrez-López, N. Masó, B. Levenfeld, A. Várez, A.R. West, *J. Am. Ceram. Soc.* **99**, 2327 (2016)
16. Q. Yu, Y. Su, R. Tursun, J. Zhang, *RSC Adv.* **9**, 13173 (2019)
17. D.G. Chen, X.G. Tang, Q.X. Liu, Y.P. Jiang, C.B. Ma, R. Li, *J. Appl. Phys.* **113**, 214110 (2013)
18. N.N. Jiang, Y. Yang, Y.X. Zhang, J.P. Zhou, P. Liu, C.Y. Deng, *J. Magn. Magn. Mater.* **401**, 370 (2016)
19. D.K. Pradhan, P. Misra, V.S. Puli, S. Sahoo, D.K. Pradhan, R.S. Katiyar, *J. Appl. Phys.* **115**, 243904 (2014)
20. S. Mukherjee, S. Pradip, A.K. Mishra, D. Das, *Appl. Phys. A* **116**, 389 (2014)
21. M.V.S. Kumar, G.J. Shankarmurthy, E. Melagiriappa, K.K. Nagaraja, H.S. Jayanna, M.P. Telenkov, *J. Mater. Sci.* **29**, 12795 (2018)
22. B.P. Rao, P.S.V.S. Rao, K.H. Rao, *IEEE Trans. Magn.* **33**, 4454 (1997)
23. R. Kumar, H. Kumar, R.R. Singh, P.B. Barman, *J. Sol-Gel Sci. Technol.* **78**, 566 (2016)
24. S. Gubbala, H. Nathani, K. Koizol, R.D.K. Misra, *Physica B* **348**, 317 (2004)
25. B.P. Rao, O.F. Caltun, *J. Adv. Mater.* **8**, 995 (2006)
26. S. Thakur, S.C. Katiyar, M. Singh, *J. Magn. Magn. Mater.* **321**, 1 (2009)
27. R. Kumar, H. Kumar, M. Kumar, R.R. Singh, P.B. Barman, *J. Supercond. Nov. Magn.* **28**, 3557 (2015)
28. L.Z. Li, L. Peng, X.H. Zhu, D.Y. Yang, *J. Electron. Sci. Technol.* **10**, 88 (2012)
29. S.L. Pereira, H.D. Pfannes, A.A.M. Filho, L.C.B. Pinto, M.A. Ch'ncaro, *Mater. Res.* **2**, 231 (1999)
30. M.A. Ali, M.M. Uddin, M.N.I. Khan, F.U.Z. Chowdhury, S.M. Haque, *J. Magn. Magn. Mater.* **424**, 148 (2017)
31. A.V. Knyazev, I. Zakharchuk, E. Lähderanta, K.V. Baidakov, S.S. Knyazeva, I.V. Ladenkov, *J. Magn. Magn. Mater.* **435**, 9 (2017)
32. Y. Ichianagi, T. Uehashi, S. Yamada, *Phys. Status Solidi* **12**, 3485 (2004)
33. Z. Zheng, Q. Feng, Q. Xiang, Z. Di, V.G. Harris, *J. Appl. Phys.* **121**, 063901 (2017)
34. K.H. Maria, U.S. Akther, I.N. Esha, M.S. Hossain, M.N.I. Khan, *J. Supercond. Nov. Magn.* **33**, 2133 (2020)
35. J.B. Nelson, D.P. Riley, *Proc. Phys. Soc.* **57**, 160 (1994)
36. T.R. Tatarchuk, M. Bououdina, N.D. Paliychuk, I.P. Yaremiy, V.V. Moklyak, *J. Alloys Compd.* **694**, 777 (2017)
37. A. Ahlawat, V.G. Sathe, V.R. Reddy, A. Gupta, *J. Magn. Magn. Mater.* **323**, 2049 (2011)
38. H. Jalili, B. Aslibeiki, A.G. Varzaneh, V.A. Chernenko, *Beilstein J. Nanotechnol.* **10**, 1348 (2019)
39. B. Aslibeiki, P. Kameli, H. Salamati, G. Concas, M.S. Fernandez, A. Talone, G. Muscas, D. Peddis, *Beilstein J. Nanotechnol.* **10**, 856 (2019)
40. J.C. Debnath, R. Zeng, D.P. Chen, S.X. Dou, *Mater. Sci. Eng. B* **177**, 48 (2012)
41. D. Li, Y.D. Huang, N. Sharma, Z.X. Chen, D.Z. Jia, Z.P. Guo, *Phys. Chem. Chem. Phys.* **14**, 3634 (2012)
42. P. Yanga, Z. Liua, H. Qia, Z. Penga, X. Fu, *Ceram. Int.* **45**, 13685 (2019)
43. F.T.Z. Toma, I.N. Esha, M.A. Amin, M.N.I. Khan, K.H. Maria, *J. Ceram. Process. Res.* **18**, 701 (2017)
44. B.C. Das, F. Alam, A.K.M.H. Akther, *J. Phys. Chem. Solids* **142**, 109433 (2020)
45. K.R. Babu, K.R. Rao, B.R. Babu, *J. Magn. Magn. Mater.* **434**, 118 (2017)

46. R. Waldron, Phys. Rev. **99**, 1727 (1955)
47. T. Gutul, E. Rusu, N. Condur, V. Ursaki, E. Goncarenco, P. Vlazan, Beilstein J. Nanotechnol. **5**, 402 (2014)
48. G.S. Shahane, A. Kumar, M. Arora, R.P. Pant, K. Lal, J. Magn. Magn. Mater. **322**, 1015 (2010)
49. V.A. Potakova, N.D. Zverve, V.P. Romanov, Phys. Status Solidi. **12**, 673 (2010)
50. I.W. Chen, X.H. Wang, Nature. **404**, 168 (2000)
51. H. Su, X. Tang, H. Zhang, Z. Zhong, J. Shen, J. Appl. Phys. **109**, 07A501 (2011)
52. M. Mahmoudi, M. Kavanlouei, J. Magn. Magn. Mater. **384**, 276 (2015)
53. S.B. Patil, R.P. Patil, J.S. Ghodake, B.K. Chougule, J. Magn. Magn. Mater. **350**, 179 (2014)
54. D. Md, T. Rahaman, R. Nusrat, A.K.M.A. Maleque, Hossain, J. Magn. Magn. Mater. **451**, 391 (2018)
55. J.S. Ghodake, R.C. Kambale, S.D. Kulkarni, S.R. Sawant, S.S. Suryavanshi, Smart Mater. Struct. **18**, 125009 (2009)
56. P.V. Reddy, T.S. Rao, J. Less Common Met. **86**, 255 (1982)
57. A. Anwar, A. Akter, M.N.I. Khan, AIP Adv. **10**, 045307 (2020)
58. M.A. Omar, *Elementary of Solid State Physics*, 2nd edn. (Wesley, Singapore, 2001)
59. J.P. Srivastava, *Elements of solid state physics* (Prentice Hall India Pvt, New Delhi, 2004)
60. S. Joshi, M. Kumar, S. Chhoker, A. Kumar, M. Singh, J. Magn. Magn. Mater. **426**, 252 (2017)
61. M.D. Hossain, M.N.I. Khan, A. Nahar, M.A. Ali, M.A. Matin, S.M. Hoque, M.A. Hakim, A.T.M.K. Jamil, J. Magn. Magn. Mater. **497**, 165978 (2020)
62. M.A. Iqbal, M.U. Islam, I. Ali, M.A. Khan, I. Sadiq, I. Ali, J. Alloys Compd. **586**, 404 (2014)
63. H.S.M. Rahimi, P. Kamelii, M. Ranjbar, H. Hajhashemi, J. Mater. Sci. **48**, 2969 (2013)
64. A. Pradeep, P. Priyadharsini, G. Chandrasekaran, J. Alloys Compd. **509**, 3917 (2011)
65. T.S. Laverghetta, *Modern Microwave Measurements and Techniques* (Artech House, London, 1988)
66. A. Rana, O.P. Thakur, V. Kumar, Mater. Lett. **65**, 3191 (2011)
67. D.L. Sekulic, Z.Z. Lazarevic, M.V. Sataric, C.D. Jovalekic, N.Z. Romcevic, J. Mater. Sci. **26**, 1291 (2015)
68. M. Hashim, S. Alimuddin, B. Kumar, H. Koo, S.E. Shirsath, E.M. Mohammed, J. Shah, R.K. Kotnala, H.K. Choi, H. Chung, R. Kumar, J. Alloy Compd. **11**, 518 (2012)
69. G.E. Pike, Phys. Rev. B **6**, 1572 (1972)
70. M.A. El Hiti, J. Phys. D Appl. Phys. **29**, 501 (1996)
71. C.G. Koop, Phys. Rev. **83**, 121 (1951)
72. J.C. Maxwell, *Electricity and Magnetism*, vol. 1 (Oxford University Press, Oxford, 1929)
73. K.W. Wagner, Arch. Elektrotechnol. **2**, 371 (1914)
74. S.A. Mazen, A.S. Nawara, N.I. Abu-Elsaad, Ceram. Int. **47**, 9856 (2021)
75. M. Younas, M. Nadeem, M. Atif, R. Grossinger, J. Appl. Phys. **109**, 093704 (2011)
76. B. Baruwati, K.M. Reddy, S.V. Manorama, R.K. Singh, O. Parkash, Appl. Phys. Lett. **85**, 2833 (2004)
77. S. Aman, N. Ahmad, S. Manzoor, M.M. Alanazi, S.A.M. Abdelmohsen, R.Y. Khosa, A.G. Al-Sehemi, R. Hua, H.A. Alzahrani, A.H. Chughtai, Catal. Surv. Asia. **27**, 165 (2023)
78. A. Kumar, B.P. Singh, R.N.P. Choudhary, A.K. Thakur, Mater. Chem. Phys. **99**, 150 (2006)
79. B. Behera, P. Nayak, R.N.P. Choudhary, J. Alloys Compd. **436**, 226 (2007)
80. M.A.L. Nobre, S. Lanfredi, Mater. Lett. **47**, 362 (2001)
81. E.V. Ramana, S.V. Suryanarayana, T.B. Sankaram, Mater. Res. Bull. **41**, 1077 (2006)
82. R.K. Kotnala, M.A. Dar, V. Verma, A.P. Singh, W.A. Siddiqui, J. Magn. Magn. Mater. **322**, 3714 (2010)
83. N.G. McCrum, B.E. Read, G. Williams, *Anelastic and Dielectric Effects in Polymeric Solids* (Wiley, New York, 1967), p. 617
84. C. León, M.L. Lucía, J. Santamaría, Phys. Rev. B **55**, 882 (1997)
85. R. Richert, H. Wagner, Solid State Ion. **105**, 167 (1998)
86. G.E. El-Falakya, O.W. Guirguisa, N.S.A. El-Aal, Prog. Nat. Sci. **22**, 86 (2012)
87. K.P. Padmasree, D.K. Kanchan, A.R. Kulkarni, Solid State Ion. **177**, 475 (2006)
88. B.V.R. Chowdari, R. Gopalakrishnan, Solid State Ion. **23**, 225 (1987)
89. S.K. Barik, P.K. Mahapatra, R.N.P. Choudhary, Appl. Phys. A **85**, 199 (2006)
90. J.R. Macdonald, *Impedance Spectroscopy: Emphasizing Solid State Material and Systems* (Wiley, New York, 1987), pp. 317–339
91. P.N. Hai, S. Ohya, M. Tanaka, Nat. Nanotechnol. **5**, 593 (2010)
92. H.K. Patel, S.W. Martin, Phys. Rev. B **45**, 10292 (1991)
93. M.B. Hossen, A.K.M.A. Hossain, Adv. Mater. Lett. **6**, 810 (2015)
94. M. Veverka, Z. Jira'k, O. Kaman, K. Kní'z'ek, M. Marys'ko, E. Pollert, K. Za've'ta, A. Lanc'ok, M. Dlouha', S. Vratslav, Nanotechnology. **22**, 345701 (2011)
95. E.J. Choi, Y.K. Ahn, K.C. Song, D.H. An, B.G. Lee, K.U. Kang, J. Korean Phys. Soc. **44**, 1518 (2004)
96. G. Bertotti, *Types of Hysteresis: Hysteresis in Magnetism, Electromagnetism* (Academic Press, San Diego, 1998)
97. J.Z. Msomi, B. Ndlovu, T. Moyo, N.S.E. Osman, J. Alloy Comp. **683**, 149 (2016)
98. F.L. Zabotto, A.J. Gualdi, J.A. Eiras, A.J.A. de Oliveira, D. Garcia, Mater. Res. **15**, 428 (2012)
99. S. Kumar, T. Shinde, P. Vasambekar, Int. J. Appl. Ceram. Technol. **12**, 851 (2015)
100. D. Varshney, K. Verma, Mater. Chem. Phys. **140**, 412 (2013)
101. A. Globus, P. Duplex, IEEE Trans. Magn. **2**, 441 (1996)
102. T. Tsutaoka, M. Ueshima, T. Tokunaga, J. Appl. Phys. **78**, 3983 (1995)
103. A.P. Grefler, V. Nakada, H. Lessoff, J. Appl. Phys. **32**, S382 (1961)
104. A. Beitollani, M. Hoor, J. Mater. Sci. **14**, 477 (2003)
105. A. Saini, A. Thakur, P. Thakur, J. Mater. Sci. **27**, 2816 (2016)

Publisher's Note Springer Nature remains neutral with regard to jurisdictional claims in published maps and institutional affiliations.

Springer Nature or its licensor (e.g. a society or other partner) holds exclusive rights to this article under a publishing agreement with the author(s) or other rightsholder(s); author self-archiving of the accepted manuscript version of this article is solely governed by the terms of such publishing agreement and applicable law.